Imperial College London

Development and characterization of a novel scintillating fibre detector for use in a proton beam therapy facility (LhARA).

Name: Vania Lay

Student CID: 01728779

Project Code: HEPH-Long-1

Supervisor: Prof. Kenneth Long

Assessor: Dr. Jaroslaw Pasternak

Word Count: 9921

September - May 2023

Submitted as part of the FHEQ Level 7 module PHYS70002 – Physics MSci Project 2022-2023
in the Department of Physics at Imperial College London

Shining a Positive Light on Dosimetry: The Future of Scintillating Fibre Detectors

Cancer is a global leading cause of death, affecting millions of people each year. One of the most common treatments is radiotherapy, which uses high-energy photons to damage cancerous cells. However, this treatment can also harm healthy tissue, increasing the risk of secondary returning cancers. Proton Beam Therapy (PBT) is a newer treatment that uses protons instead of photons to target tumours. PBT has been shown to be more effective and less damaging to healthy tissue than traditional radiotherapy. However, there are currently only two operational PBT facilities in the UK, making it expensive and difficult to access for many patients.

This is where the LhARA project comes in. LhARA (the Laser-hybrid Accelerator for Radiobiological Applications) is working to create a novel research facility capable of delivering PBT. The project aims to position PBT as a viable, economical treatment option for patients by reducing facility size and incorporating novel technology and developments in physics.

Accurate measurements of dose (also known as dosimetry) are crucial for the realization of commercial PBT as they provide valuable information used for ensuring the quality of patient treatment delivery. The SmartPhantom is being developed as a real-time measurement system to ensure that dose is carefully monitored and delivered to the patient throughout treatment, maximising tumour irradiation and minimizing healthy tissue damage. Our project focuses on creating a functional prototype of the SmartPhantom's scintillating fibre (SciFi) detectors, which will be used to accurately measure the real-time dose deposited by an incoming proton beam.

To test the effectiveness and accuracy of the SciFi detectors, we created a simulation to replicate detector dose measurements. The measurements were then used to successfully reconstruct the beam’s depth-dose distribution using an analytical fit, providing information on where and how much dose is delivered to the patient. Two SciFi detector prototypes were also designed and built for the project. The first prototype was judged unsuccessful as it was very difficult to construct and suffered from extreme alignment issues, making it incapable of accurately measuring energy deposition. The second prototype was considerably improved, with the new construction method resulting in a more accurate detector which was later tested with an ultraviolet source.

The SmartPhantom is an exciting project that has the potential to revolutionize the way we measure dose. It could significantly improve the accuracy and quality of patient treatment delivery, making PBT a more accessible and viable treatment option for cancer patients. The SciFi detectors are a vital component of the SmartPhantom, and this project has been a steppingstone for their development. We hope that our work will inform future developments for the SciFi detectors and SmartPhantom, and ultimately, contribute to the advancement of real-time dose measurements and LhARA's mission to provide accessible PBT for everyone!

Abstract

Proton beam therapy (PBT) is a rapidly advancing cancer treatment scheme that delivers highly localized radiation to cancerous cells whilst minimizing damage to healthy tissue. Accurate dosimetry is crucial for effective treatment planning and dose calibration, and the SmartPhantom is a promising solution for real-time measurement of irradiation dose and 3D beam profile reconstruction. In this project, functional prototypes of the scintillating fibre (SciFi) detectors for the SmartPhantom were developed and assessed through three stages: simulation, manufacturing, and testing. A Geant4 simulation was expanded to produce simulated SciFi detector energy deposition measurements, which were used to reconstruct the depth-dose distribution of a 20 MeV proton beam with a Bortfeld analytical model. This resulted in a 98.3% reconstruction accuracy and 97.2% accuracy for the reconstructed Bragg peak distance compared to the equivalent NIST database value. A mark I design was developed; however, alignment issues and labour-intensive production resulted in an unsuccessful prototype. A mark II prototype was then created using a winding jig to improve alignment. Following its successful construction, the prototype underwent testing, achieving a 74.2% pitch accuracy. The prototype was used to reconstruct the depth-dose distribution of an ultraviolet source. This work demonstrates progress towards the development of a reliable SmartPhantom, which could improve the accuracy and efficiency of PBT treatment planning and delivery.

Acknowledgements

I would like to thank my project partner. It has been a difficult and rewarding time and it would have been a lot harder without their support, hard work, and constant encouragement.

I would also like to thank Professor Ken Long for his continuous supervision and assistance. It has been an immense pleasure having him as a supervisor and his advice has been invaluable throughout the project.

I would like to thank Josie McGarrigle and Maria Maxouti for their help, guidance, and patience throughout the project.

I would also like to extend my gratitude to Oliver Jeremy and the HEP workshop, without whom the prototypes would not have been designed and manufactured.

Finally, I would like to thank the LhARA community (specifically to the ion-acoustics and LhARA-local teams) for the constant advice and support these last two terms.

Contents

Chapter 1

Introduction

In the UK, it is anticipated that 1 in every 2 people will develop cancer [1] [2]. The 19 million cases globally each year are predicted to grow to 27.5 million by 2040 propelled by the aging population alongside other socio-economic factors, indicating a vital need to develop efficient and effective cancer treatment schemes [3] [4]. There are currently many cancer therapy options available including surgery, chemotherapy, radiotherapy, and immunotherapy. After surgery, radiotherapy is the most popular treatment option, with 50% of all cancer patients receiving palliative or curative radiotherapy [5]. Radiotherapy utilises high energy particles delivered to the cancerous tumour to damage and kill its DNA structure. Proton beam therapy (PBT) – first proposed in 1946 – replaces the conventional high energy photons in X- and gamma- ray radiotherapy with protons. In contrast to photons, protons have a much sharper Bragg peak in their depth-dose distribution, meaning the energy deposited is highly localised, reducing the amount of secondary tissue damage [6].

Accurate dose measurements are vital for the realization of commercial PBT. Measuring the energy deposition is crucial to reconstructing the beam profile and dose deposition, providing key information to ensure maximum dose is delivered to the tumour and healthy tissue is spared. The SmartPhantom is being developed in conjunction with LhARA as a real-time measurement system to ensure that dose is carefully monitored and delivered to the patient. This project focuses on creating a functional prototype of the SmartPhantom's scintillating fibre (SciFi) detectors, which will be used to accurately measure the real-time dose deposited by an incoming proton beam. This project aims to simulate, design, manufacture and test a novel SciFi detector prototype. The simulation will focus on modelling the design to reproduce simulated results for the energy depositions in the detector, which will be used to reconstruct the depth-dose distribution. The experimental component will integrate various design considerations to manufacture a prototype for the detector. The design will be evaluated and assessed before the testing stage, where the prototype performance will be quantified through quality assurance procedures.

Chapter 2

Protons for Therapy

This chapter provides an overview of the mechanisms of particle-matter interactions and the benefits of PBT.

2.1 Particle-Matter Interactions

As a particle travels through matter, it gradually loses its kinetic energy, primarily through collisional excitation and ionization, until it comes to rest. The loss in kinetic energy can lead to direct and indirect ionizing radiation. Direct ionization occurs when the particle deposits enough energy to irradiate the matter. Indirect ionization arises when a neutral particle (neutron, photon etc.) collides and the resulting energy transfer liberates another particle, which will in turn, directly ionize the matter [7] [8] [9]. The energy loss per unit path length (known as the stopping power) for charged particles is proportional to the square of the particle's charge and inversely proportional to its square velocity. This signifies that the interaction cross section is inversely proportional to the particle's energy. As a particle undergoes multiple collisions and interactions, it eventually comes to rest, causing a decrease in the particle's upstream flux. This reduction of particle species over distance ultimately defines the depth-dose distribution. As protons have a larger mass and thus, lower entry energy than photons, they deposit more energy at each interval as they slow down, corresponding to a sharper depth-dose distribution.

TABLE I
SUMMARY OF PROTON-MATTER INTERACTIONS AT THERAPEUTIC ENERGIES

Interaction	Target	Products	Primary Proton Effect	Dosimetry
Inelastic Coulomb Scattering	Atomic electrons	Primary proton, electrons	Quasi-continuous energy loss	Range in patient
Elastic Coulomb Scattering	Atomic electrons	Primary proton, recoil nucleus	Deflection	Penumbral sharpness
Non-elastic Nuclear Reactions	Atomic electrons	Secondary proton, neutrons, heavy ions etc.	Primary proton loss	Fluence, neutron generation
Bremsstrahlung	Atomic electrons	Primary proton, photons	Energy loss, deflection	Negligible

This project will primarily concern proton-matter interactions, which can be found in Table I [10] [11] and include:

- Stopping: Occurs when protons lose energy and eventually come to rest via a series of multiple electromagnetic interactions, primarily with atomic electrons.
- Multiple Coulomb scattering (MCS): When protons are randomly deflected by electromagnetic interactions with atomic electrons and nuclei [12].
- Nuclear reactions: The single scatter of a proton by electromagnetic or nuclear forces, leading to a dose distribution at distances far from the target atom [13].

2.2 Characterization

There are two main characteristics of proton-matter interactions that influence PBT: ionization energy and range, which form the basis of the depth-dose distribution.

2.2.1 Energy

Dosimetry concerns the measurements and calculations of energy deposition within matter and can be described using various dosimetric quantities such as the following [14, 15]:

- Fluence, φ: The number of protons, *N*, incident on a small sphere of infinitesimal area, *dA*.

$$\varphi = \frac{dN}{dA}. \quad (2.1)$$

- Energy fluence, ψ: The radiant energy, $dE_{kin,}$ incident on a small sphere of infinitesimal area, *dA*.

$$\psi = \frac{dE_{kin}}{dA} = \varphi E_{kin}. \quad (2.2)$$

- Mass stopping power, $\frac{dE}{dx}$: Stopping power over the density of an absorbing medium. The mean energy loss of a charged is given by the Bethe-Bloch formula (constants defined in Table II) [16]:

$$-\frac{dE}{dx} = Kz^2\frac{Z}{A}\frac{1}{\beta^2}\left[\frac{1}{2}\ln\left(\frac{2m_e c^2\beta^2\gamma^2 T_{max}}{I^2}\right) - \beta^2 - \frac{\delta(\beta\gamma)}{2}\right]. \quad (2.3)$$

- Absorbed Dose, *D*: Average energy lost by ionizing radiation to an absorbing medium (mass, *m*).

$$D = \frac{d\bar{E}}{dm}. \quad (2.4)$$

By combining these terms alongside dimensional analysis, dose can be related to fluence (Φ) and stopping power $\left(\frac{S}{\rho}\right)$:

$$D = \frac{energy}{mass} = -\frac{\left(\frac{dE}{dx}\right) \times dx \times dN}{\rho \times dA \times dN} = \Phi\frac{S}{\rho}. \quad (2.5)$$

TABLE II
DEFINING BETHE-BLOCH FORMULA VARIABLES AND CONSTANTS

Variable / Constant	Value
K	$4\pi N_A r_e^2 m_e c^2$
N_A	Avogadro constant
r_e ,m_e	Classical electron radius and mass
c	Speed of light
z	Charge of incident particle
Z, A	Atomic number and weight of absorber material
β	v/c
γ	Lorentz factor
$\delta(\beta\gamma)$	Density effect correction due to polarization
I	Mean excitation energy

2.2.2 Range

The range describes the distance a charged particle travels through a medium before coming to rest. As a particle traverses a medium, it interacts with multiple electrons and each time, loses a small fraction of its incident kinetic energy. This incremental energy loss means that the particle does not stop at the same depth each time (known as range straggling). The average path length travelled by the charged particle can be estimated using the continuous slowing down approximation as in (2.6), which assumes that the rate of energy loss at each point along the track is equal to the total stopping power [8].

$$R_{CSDA} = \int_0^{T_0} \left[\frac{S(E)}{\rho}\right]^{-1} dE. \quad (2.6)$$

Proton energy loss and range are often measured in terms of water-equivalence as water and tissue have similar densities and effective Z/A. At high energies, the energy, E, logarithm and range, R, appear linear shown in (2.7), known as the Bragg-Kleeman rule where α is a material dependant constant and p is an energy dependent parameter.

$$R = \alpha E^p. \quad (2.7)$$

2.2.3 Bragg Curve

The Bragg curve is the depth-dose distribution illustrating the ionization energy of a particle at different depths, arising from the combination of stopping, scattering and nuclear reaction effects.

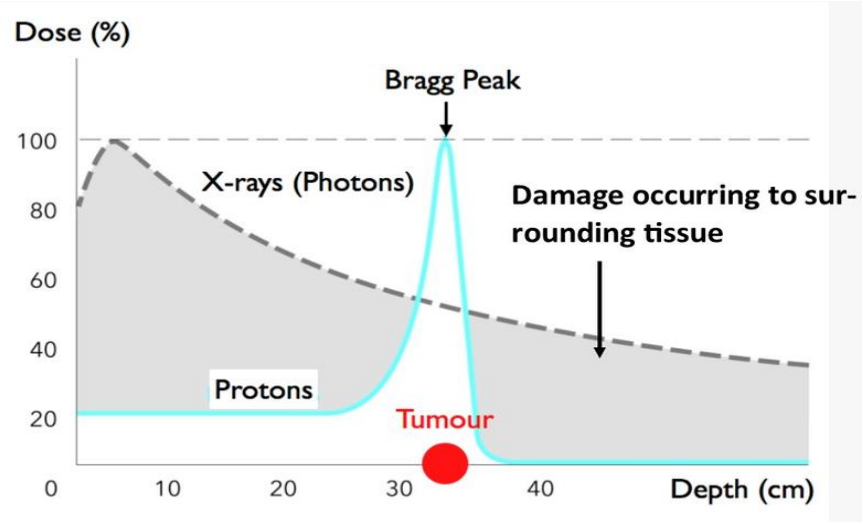

Fig. 2.1: The depth-dose distribution for protons (blue) compared to photons (grey) showing a more localised proton dose deliverance to the tumour. Taken from [17].

In Fig. 2.1, the solid blue line clearly shows the characteristic Bragg peak of a proton, the point at which most of the particle's energy is deposited. Eqn. 2.7 shows the dependence of Bragg peak depth on beam energy – as a particle slows down, its stopping power increases corresponding to a rise in Bragg peak depth. Thus, the Bragg peak can be calibrated to precisely target the tumour depth by varying beam energy.

The Bragg curve is important for treatment planning, as it can inform dose requirements. It can be approximated using Bortfeld's model (a closed form analytical Bragg curve approximation) which uses Gaussian and parabolic cylinder functions to model [18]:

- Energy-Range dependence: The Bragg-Kleeman rule.
- Fluence Reduction due to nonelastic nuclear interactions: Linear model.
- Range Straggling: Gaussian approximation.
- Energy spectrum of poly-energetic beams: Gaussian approximation with a linear "tail."

TABLE III
DEFINING BORTFELD'S MODEL PARAMETERS

Parameter	Definition	Value	Units
p	Range-energy relation exponent	1.77	
α	Proportionality factor	0.0022	cm MeV^{-p}
R_0	Range	E_0^p	cm
β	Fluence-reduction relation slope	0.012	cm^{-1}
γ	Fraction of locally absorbed energy released in nonelastic nuclear interactions	0.6	
σ_{mono}	Gaussian range straggling width	$0.012\ R_0^{0.935}$	cm
$\sigma_{E,0}$	Gaussian energy spectrum width	$\approx 0.01\ E_0$	MeV
ε	Fraction of primary fluence contributing to energy spectrum tail	≈ 0.0 - 0.2	

This model is applicable to protons with energies between 10 and 200 MeV and its parameters (Table III [10]) can be combined to form the full equation:

$$D(z) \approx \begin{cases} \Phi_0 \dfrac{(R_0 - z)^{\frac{1}{p}-1} + (\beta + \gamma\beta p)(R_0 - z)^{\frac{1}{p}}}{\rho p \alpha^{\frac{1}{p}}(1 + \beta R_0)}, & z < R_0 - 10\sigma \\ \Phi_0 \dfrac{e^{-\frac{\varsigma^2}{4}} \sigma^{\frac{1}{p}} \Gamma\left(\frac{1}{p}\right)}{\sqrt{2\pi} p \rho \alpha^{\frac{1}{p}}(1 + \beta R_0)} \left[\frac{1}{\sigma}\mathfrak{D} - \frac{1}{p}(-\varsigma) + \left(\frac{\beta}{p} + \gamma\beta + \frac{\epsilon}{R_0}\right)\mathfrak{D} - \frac{1}{p} - 1(-\varsigma)\right], & R_0 - 10\sigma \le z \le R_0 + 5\sigma \\ 0, & otherwise \end{cases} \quad (2.8)$$

where Φ_0 is primarily fluence, ρ is medium density, E_0 is beam energy, $\Gamma\left(\frac{1}{p}\right) = 1.575$ is the gamma function and,

$$\sigma^2 = \sigma_{mono}^2 + \sigma_{E,0}^2 \alpha^2 p^2 E_0^{2p-2}, \quad (2.9)$$

$$\varsigma = \frac{R_0 - z}{\sigma}. \quad (2.10)$$

2.3 Benefits and Importance of PBT

When ionising radiation is delivered to a tumour, it causes DNA lesions which damages cancer cell structure [19]. This damage can include double-strand breaks which are effective in preventing DNA repair pathways, leading to genome instability, DNA aberration formation and cell death [7] [6] [20]. Thus, radiation therapy is an effective cancer treatment option. Currently, the most popular radiation sources are photon beams; however, there are many limitations, the most significant being the difficulty in precisely honing dose deliverance. This stems from the indirect ionization effects of photons being more difficult to isolate onto targets as shown in Fig. 2.1, where the depth-dose distribution for photons (shown in grey) has a very large width and lacks the characteristic Bragg peak [21]. This is due to the larger range of photons within matter corresponding to a higher penetrating dose depth and thus, radiation being unnecessarily delivered to healthy tissue outside of the target volume [22].

PBT uses protons in the place of photons to deliver radiation to tumour cells [23]. The use of protons exploits the characteristic Bragg peak to deliver dose to precise target volumes, minimising damage to healthy tissue [24]. PBT is also highly adaptable to different tumour sizes and shapes as, in conjunction with medical imaging techniques, the dose can be calculated in three-dimensional space to maximise dose deliverance by utilising multiple beams and beam energies to effectively target the cancer [25]. Thus, PBT is a highly effective treatment option; however, its novelty and relative youth makes it currently, an expensive and under-researched alternative [26] [27].

Chapter 3

Dosimetry

This chapter will discuss current dosimetric methods and in particular, two techniques for proton beam dosimetry: scintillating fibres and ion-acoustics.

3.1 Current Dosimetric Methods

The understanding of charged particle - tissue interaction is pivotal in the realization of commercial PBT. It is important that the dose profile measurements of irradiated cells are accurate to maximize cancerous tissue irradiation, minimize healthy tissue damage and improve dose calibration [28].

Standard dosimetry methods utilize detectors positioned at the location of biological samples to measure dose. However, these methods have two key limitations: the need to conduct the measurements separately to the biological sample irradiation and the partial measurement of integrated dose over the area, both leading to uncertainty in dose deliverance stemming from the beam distribution variations over time [29].

There are currently many different methods for measuring the dose of a proton beam including:

1. Proton emission tomography (PET): A PET scan taken immediately during or after irradiation can image the signal of short-lived positron emitting isotopes created when protons interact with tissue. This method is unable to explicitly map the Bragg peak as the inelastic scattering within the tissue increases the overall signal, corresponding to a ‘clipped’ Bragg peak. This technique can be used both online and offline. Online imaging suffers from reduced detector sensitivity and field of vision which, alongside the difficulties surrounding the beam and detector orientation, interferes with accurate 3D image acquisition. Due to the delay in obtaining images post irradiation used for offline monitoring, the quality and intensity of signal obtained from the positron emitters decays [30].

2. Film dosimetry: By coating a transparent polymer base with a thin sensor film layer, a film dosimeter can be created which turns deep blue upon irradiation. The optical density of the blue directly correlates to the absorbed radiation dose, which can be used to map the dose of protons and heavy ions; however this technique has very low accuracy due to its inconsistency in radiation detection [31] [32].
3. Ionisation chambers: This apparatus is the industry standard for dosimetry, where the beam is propagated through a chamber and the resultant relics stemming from interactions of the ionising radiation and matter within the chamber is detected. These chambers are highly adaptable but also require calibration to determine the deposited dose [33].

This project aims to investigate novel techniques and designs to create a real-time dosimeter with improved accuracy and functionality. By measuring dose in real-time, the information can be incorporated into live treatment planning, optimizing the patient's treatment.

3.2 Scintillating Fibres

This project concerns the development of SciFi detectors. SciFi detectors are constructed using layers of aligned scintillating fibres and are currently used in various applications such as high-energy physics, medical imaging, and radiation monitoring, due to their ability to detect and measure ionizing radiation.

Scintillating fibres can be used to detect charged particle radiation, by converting the incoming radiation into a detectable photon output. There are three main processes that generate the photon output in a scintillator [34]:

1. Fluorescence: The excitation of molecules within the scintillator followed by the immediate emission of a photon. A simplified diagram showing this mechanism can be seen in Fig. 3.1.
2. Delayed fluorescence: Follows the same process of fluorescence but with a longer period between excitation and emission.
3. Phosphorescence: Though similar to fluorescence, this process has a longer emission time, as emission continues after excitation terminates, leading to a longer emitted wavelength.

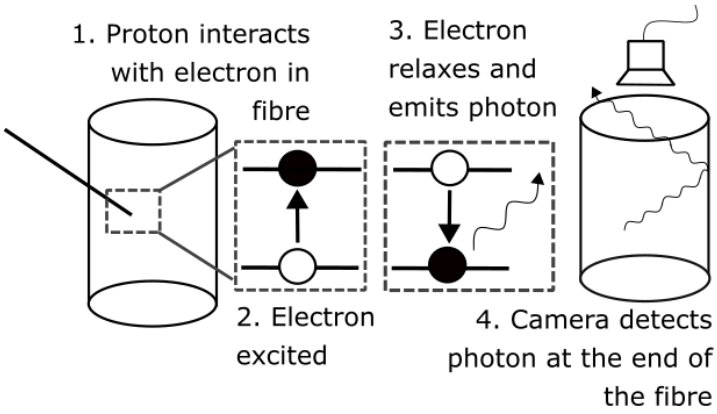

Fig. 3.1: Fluorescence mechanism behind scintillating fibre dosimetry illustrating how an incoming proton is translated to a photon output [34].

The intensity, I, of the photon output is given by:

$$I = I_o e^{-\frac{t}{\tau}}, \qquad (3.1)$$

where I_o is the maximum intensity and τ is the fluorescent decay time ($\sim$ 1 ns).

The scintillation efficiency is defined as the fraction of energy from the incident particle that is converted into a photon output. There are many factors which influence the scintillation efficiency. Primarily within the scintillator itself, there are a series of emission and self-absorption events that attenuate the photon output. Quenching – the limitation of fluorescence intensity due to unwanted effects – also degrades the photon output of a scintillator [35].

The response of a scintillator, assuming that the light yield ($\frac{dL}{dx}$) is proportional to energy loss ($\frac{dE}{dx}$) and no quenching, can be described as [34]:

$$\frac{dL}{dx} = S\frac{dE}{dx}, \quad (3.2)$$

where S is the scintillator efficiency.

To incorporate quenching, it can be assumed that scintillation efficiency is degraded by quenching from damaged molecules and that the density of said molecules is proportional to the ionisation density. Therefore, (3.2) can be modified to incorporate the fraction of undamaged scintillator molecule to give Birks' Law [36]:

$$\frac{dL}{dx} = \frac{S\frac{dE}{dx}}{1 + kB\frac{dE}{dx}}. \quad (3.3)$$

For a small $\frac{dE}{dx}$, this simplifies to (3.2). However, this equation is not applicable to protons due to their higher linear energy transfer corresponding to a non-linear response to quenching. Alternative equations have been proposed to adapt Birks' law to empirical proton data including Craun and Smith's relation [37]:

$$\frac{dL}{dx} = \frac{S\frac{dE}{dx}}{1 + kB\frac{dE}{dx} + C\frac{dE}{dx}^2}, \quad (3.4)$$

where C is an empirical constant.

By measuring the light yield of the scintillator using photomultiplier tubes or a camera, the output can be directly correlated to the incoming radiation. Therefore, SciFi detectors are an effective method for accurately measuring energy.

3.3 Ion-acoustics

The LhARA project aims to incorporate the use of ion-acoustic dosimetry to produce real-time 3D beam profile reconstructions [38]. Ion-acoustics considers the thermoacoustic pressure waves generated when ionising radiation causes local tissue heating upon energy deposition. This local temperature increase is particularly noticeable around the Bragg peak [39]. The initial pressure, $p_o(\boldsymbol{r})$, can be described as:

$$p_0(\boldsymbol{r}) = \Gamma(\boldsymbol{r})D(\boldsymbol{r})\rho(\boldsymbol{r}). \quad (3.5)$$

By assuming a short heating time and negligible thermal diffusion, a spatially and temporally varying pressure wave can be defined (all variables in Table IV):

$$\nabla^2 p(\boldsymbol{r},t) - \frac{1}{{v_s}^2}\frac{\partial^2}{\partial t^2}p(\boldsymbol{r},t) = \frac{\Gamma}{{v_s}^2}\frac{\partial}{\partial t}D(\boldsymbol{r},t)\rho(\boldsymbol{r}). \quad (3.6)$$

TABLE IV
DEFINING ION-ACOUSTIC FORMULA PARAMETERS

Parameter	Definition
$p_o(\mathbf{r})$	Initial pressure at given location r
$\Gamma(\mathbf{r})$	Grünesian parameter: Energy to pressure conversion efficiency
$D(\mathbf{r})$	Dose deposition of beam at given range r
$\rho(\mathbf{r})$	Medium density
$p(\mathbf{r},t)$	Pressure at a given distance, r, and time, t
v_s	Speed of sound in the medium

This relationship means that the Bragg peak position and relative dose can be inferred from the reconstruction of the initial pressure, whilst the absolute dose can be calculated using known medium properties. As such, the correlation allows the determination of dose at different ranges using algorithms such as universal back projection, Fourier transform, iterative time reversal and inverse Radon transforms. In conjunction with ultrasound imaging, this technique can be used to produce real-time *in-vivo* images during treatment, maximising PBT benefits as dose can be monitored and adjusted accordingly. However, the limitation of this method comes from the clinically relevant proton beam energies (70-230 MeV) corresponding to ultra-low pressure and frequency amplitudes which are difficult to detect, requiring highly sensitive equipment [40] [41].

Ion-acoustics is currently a popular field of research. In particular, there is an active focus on the development of new equipment with improved sensitivity. Current research proposes a linear sensor array – comprised of 5 to 200 elements - for the dose mapping of 20 and 22 MeV proton beams in a water phantom [38]. Whilst this apparatus is able to determine an accurate Bragg peak range, the lateral resolution of the mapping is poor, with over a 10% error due to limited field of view. The research suggests that by using two imaging mechanisms simultaneously with different fields of view, the issue can be resolved whilst preserving the ability to detect signals <50 kHz [42]. Though ion-acoustics and ultrasound imaging are strong candidates for real-time *in-vivo* imaging, there is insufficient sensitivity in current equipment to make it viable for PBT. This novel research is pivotal in advancing ion-acoustic dosimetry capability and is informative to the development of the LhARA project.

Chapter 4

LhARA

This chapter includes an overview of the project in the context of LhARA and the SmartPhantom.

4.1 LhARA Overview

The LhARA (Laser-hybrid Accelerator for Radiobiological Applications) project is a collaboration aiming to create a facility capable of delivering innovative particle beam therapy regimes, combining several ion species (i.e. proton and carbon) into a single treatment and employing ultra-high dosage and temporal-, spatial- and spectral-fractionation schemes to maximise treatment performance. The system will deliver patient tailored real-time treatment. LhARA aims to reduce the cost of PBT by targeting the system size to ensure PBT can become a more viable, economical treatment option for patients. The project seeks to create a facility capable of delivering highly flexible infrastructure to support and foster research into the radiobiological effects of PBT [43] [44].

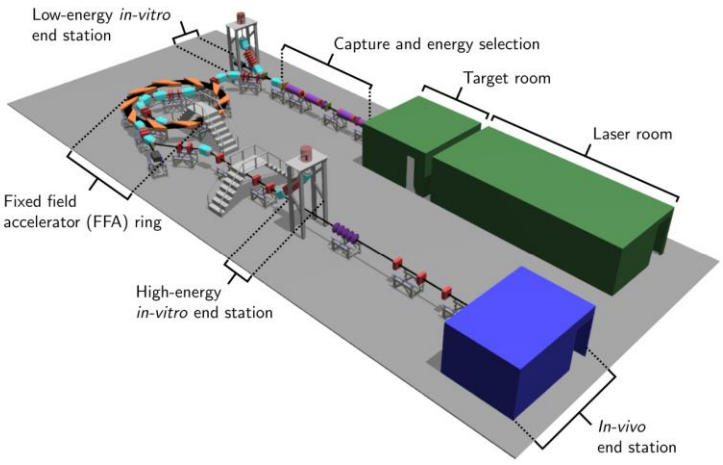

Fig. 4.1: A full diagram of the proposed LhARA facility taken from [44].

LhARA is currently being developed to serve the Ion Therapy Research Facility (ITRF) and works by exploiting laser beams to create large fluxes of protons/ions which can be captured and honed into beams using strong-focusing plasma (Gabor) lenses. This method allows the current space-charge limit on instantaneous dose rate typically found at other conventional facilities to be circumvented, producing captured protons and ions with significantly higher energies. The laser driven source also provides flexibility in the beam's energy, time, and spatial structure, preserved using a fixed field alternating gradient accelerator (FFA) for post-acceleration. A diagram of the full LhARA system can be seen in Fig 4.1.

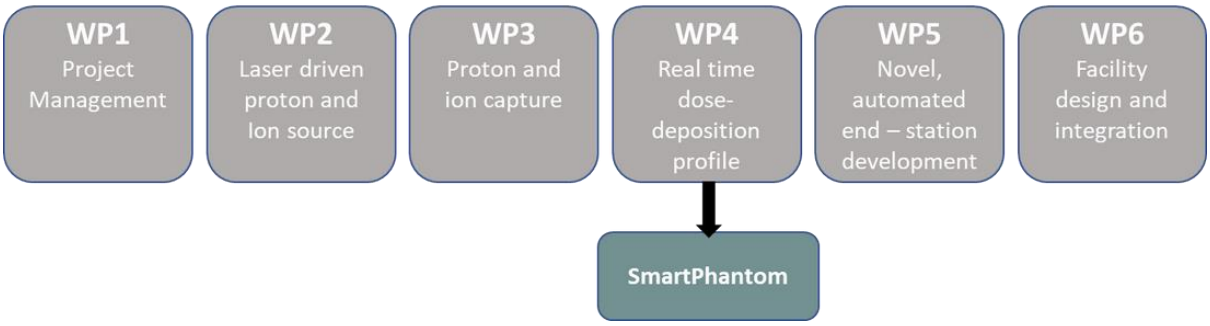

Fig. 4.2: A diagram illustrating the six LhARA work packages adapted from [44].

The LhARA project is split into six primary work packages which can be seen in Fig. 4.2. The focus of this project is on work package four concerning the development of the SmartPhantom. The fourth work package explores the creation of a mapping system capable of tracking real-time dose-deposition using ion-acoustics and SciFi detectors, aiming to provide in-vivo real-time 'ion-acoustic dose localisation and quantitative mapping' [43]. The SmartPhantom will be a transportable, compact device capable of measuring the energy deposited by an incoming proton beam using SciFi detectors, with the results informing the development of ion-acoustic imaging apparatus [29].

4.2 SmartPhantom

4.2.1 Motivation

To address the issues of current dosimetry methods illustrated in the previous chapter, the SmartPhantom is currently being developed as a method of producing real-time measurements of irradiation dose capable of 3D beam reconstruction. To simulate the irradiation of cells and measure the according dose profile, a water phantom is used to emulate soft tissue and muscle. The SmartPhantom will utilize SciFi detectors placed at various depths within the water phantom alongside detailed simulations to measure dose and dose uniformity [29].

4.2.2 Design

The SmartPhantom (shown in Fig. 4.3) is a water phantom which includes several SciFi detectors situated in front of the sample that when irradiated, will measure the energy deposition as a function of its position.

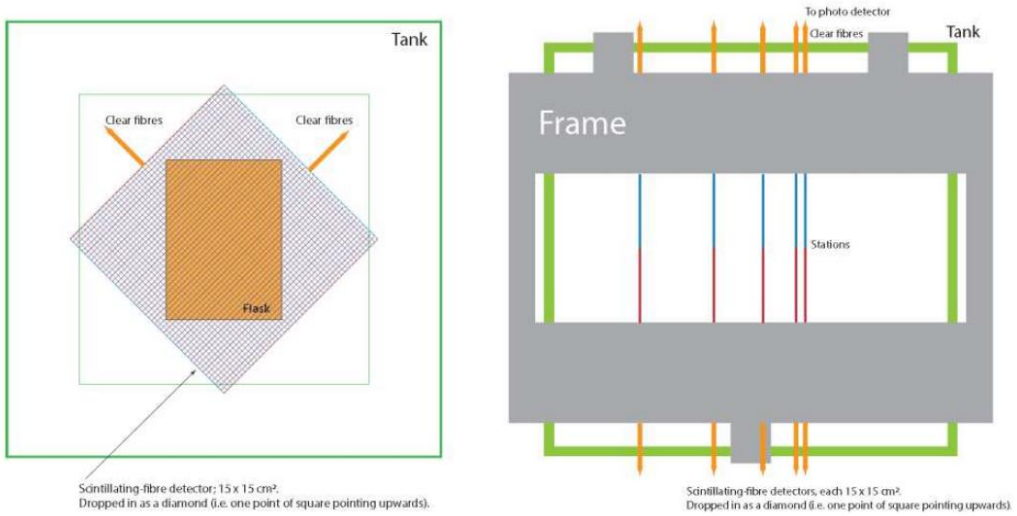

Fig. 4.3: Initial schematic diagrams of SmartPhantom designed for use at MedAustron taken from [29]. Left is the beam's eye view and right is the top-down view.

By combining these measurements with simulations, the location and dose of the Bragg peak can be determined. The scintillating fibre cores are made of polystyrene which has a similar density to water, to mitigate any shift in Bragg peak due to the detector. Each fibre station contains two perpendicular SciFi detectors providing 2D intensity profile information, used to calculate the location of the Bragg peak at each x-y position. Using clear fibres connected to the scintillating fibres, the photons will be transferred out of the water, the output captured via camera and converted to coherent measurements using image processing software. By measuring the dose profile simultaneously while irradiating the biological sample, uncertainty in dose due to beam variation is eliminated.

4.2.3 Development

Geant4 simulations were used to model the geometry of the SmartPhantom [10]. The simulation confirmed that the SciFi detectors had a negligible effect on energy deposition at the Bragg peak for proton beams of various energies. However, water equivalence assessments for the scintillating fibres showed that there was a noticeably higher deposition in the detectors compared to water due to the mylar films used to model the detector, which saw increased linear energy transfer. Thus, a conversion factor was necessary to correct for this and Bortfeld's model was fitted to the adjusted simulation data, shown in Fig. 4.4.

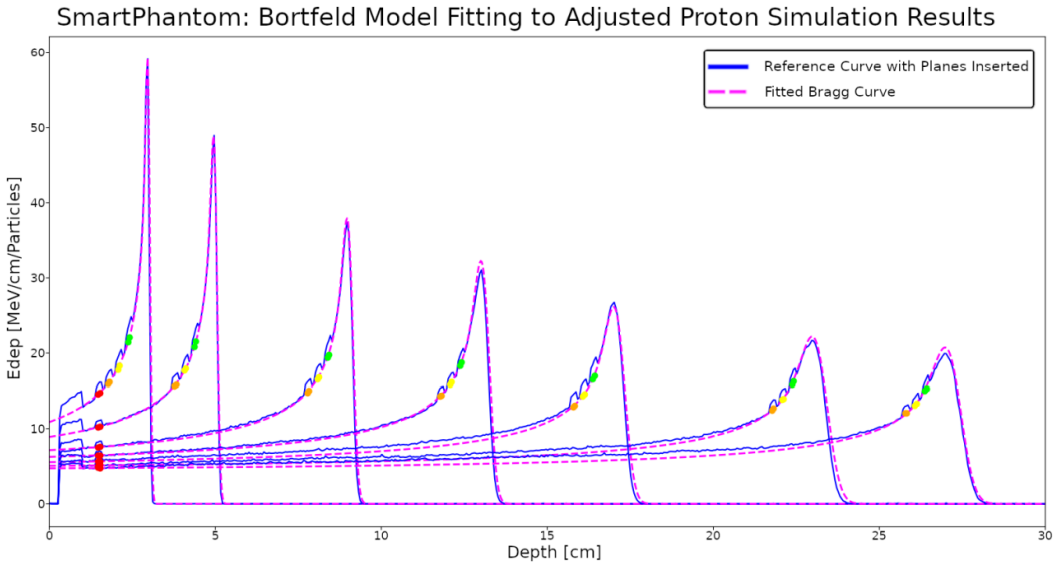

Fig. 4.4: Fitted Bortfeld's model (pink) to adjusted simulation results (blue) for several beam energies. Taken from [10].

The scintillating fibre bundles were also assessed to determine the camera readout and software needed for the SmartPhantom. The bundles (shown in Fig. 4.5) were evaluated with ultraviolet light, which concluded that:

- Mapping for each detector was needed to correlate readout to scintillating fibres.
- Flood filled algorithm was needed to distinguish fibres.
- Image processing techniques was required to clean results and differentiate fibres.
- Conversion factor of pixel intensity to energy was needed.

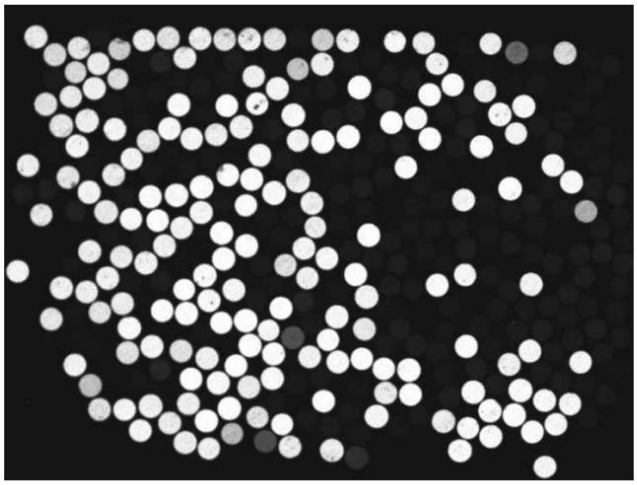

Fig. 4.5: Fibre bundle test - camera readout from scintillating fibre ends when ultraviolet source is applied. Taken from [10].

The fibres were then exposed to a proton beam to verify that a signal could be obtained. The results also served as initial proof of principle for the scintillating fibres.

This research phase concluded with four important considerations for future SmartPhantom work:

1. Revision of frame design as its structure needs to be thin to fit into the water phantom but strong enough to withstand the tension applied by the taut fibres.
2. Review of adhesive used for as it must not affect the performance of the fibres.
3. Consideration of uncovered scintillating fibres to ensure they are not exposed to external light which may impact readout.
4. Recommendation to ensure that the scintillating and clear fibres are perfectly aligned to maximise readout.

This project will continue the work on the SciFi detectors and SmartPhantom, using previous iterations and resulting considerations to inform key design elements.

Chapter 5

Simulation

This chapter describes a pre-existing Geant4 simulation which was expanded for the project and presents the simulation functions and results.

5.1 Objectives

The main objective was to expand existing Geant4 code to localise a 20MeV proton beam's dose deposition within each SciFi detector and fibre. To supplement this, a module overview of the code was created to better understand the simulation and to look at restructuring the modules for improved efficiency. The expanded simulation's SciFi detector dose deposition data was then used to reconstruct the simulated depth-dose distribution.

5.2 Geant4 Simulation

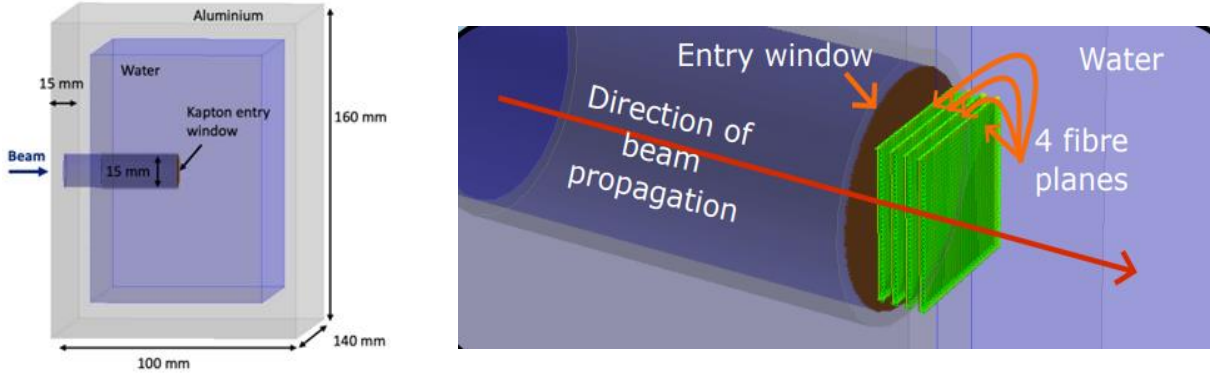

Fig. 5.1: Diagram showing the geometry of the Geant4 simulation (left) and image of the four SciFi detectors (green) in simulation (right).

The Geant4 simulation was initialised as depicted in Fig. 5.1: the water phantom is modelled as an aluminium box (15 mm thickness) containing a fixed volume (100 x 140 x 160 mm^3) of water. A proton beam propagates along the z-axis unperturbed through a cylindrical cavity of 3 cm in length until it reaches a Kapton entry window, where it enters the phantom. This entrance window is placed to ensure that the Bragg peak is located at the centre of the phantom. As the beam propagates through the phantom, it deposits energy and interacts with the four detectors, illustrated in Fig. 5.1. The energy and spatial distributions of the modelled proton beam can be seen in Figs. 5.2 and 5.3 respectively. Both graphs illustrate the predicted symmetrical distributions and in particular, the energy distribution was fit with a Gaussian of parameters $\mu = (20.000 \pm 0.004)$ and $\sigma = (-0.410 \pm 0.004)$. The proton beam average energy is 20 MeV as anticipated and the associated beam deviations in energy and space are small.

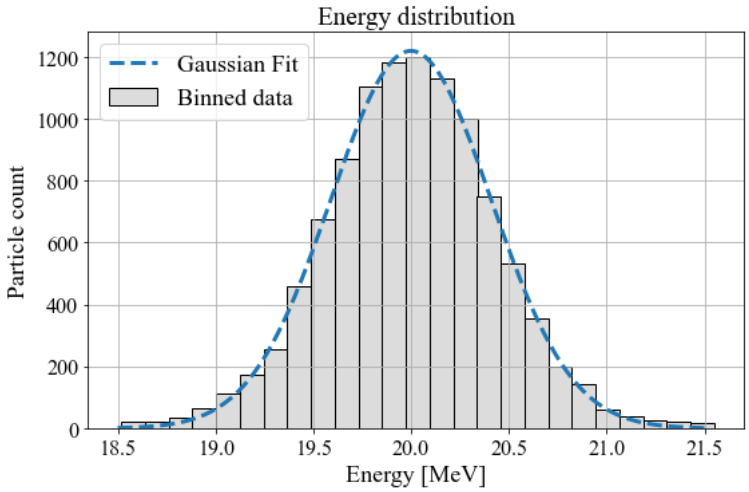

Fig. 5.2: Graph showing the energy distribution of the modelled proton beam used in the Geant4 simulation, illustrating a Gaussian distribution with the parameters $\mu = (20.000 \pm 0.004)$ and $\sigma = (-0.410 \pm 0.004)$.

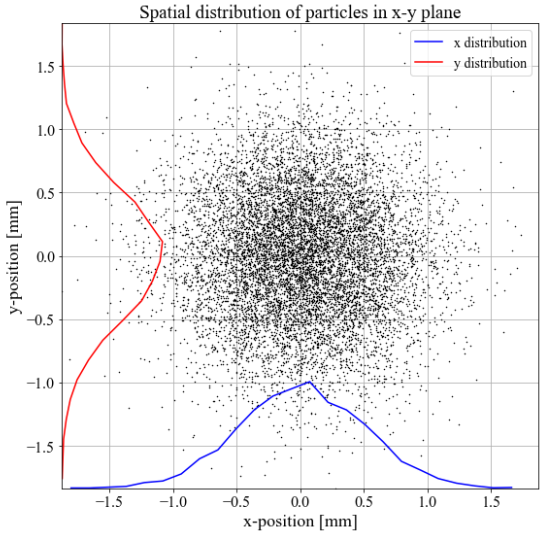

Fig. 5.3: Graph showing the x-y spatial distribution of the particles in the modelled proton beam.

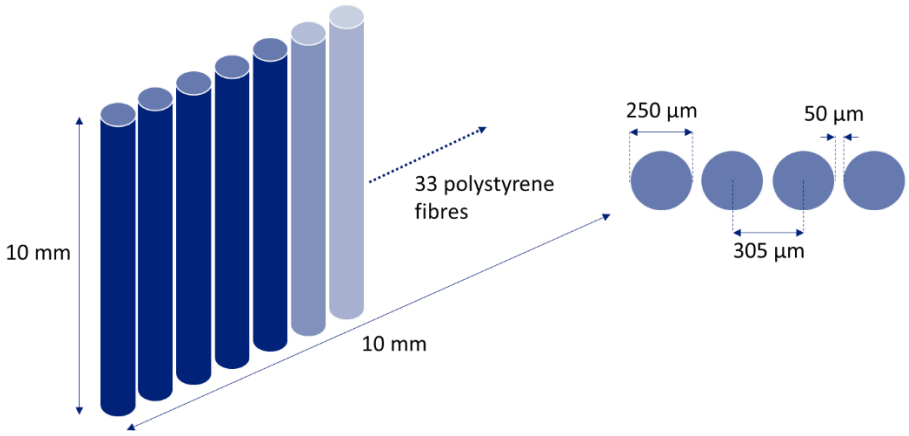

Fig. 5.4: Diagram showing scintillating fibre geometry and dimensions – 33 250 µm fibres are arranged with a 305 µm pitch. Off-axis view of a few fibres (left) and top-down view of fibres (right).

The SciFi detectors are modelled as polystyrene, with their optical properties including Birks' constant and scintillation and transmission efficiencies being manually defined in the initialisation process. As shown in Fig. 5.4, each detector consists of thirty-three fibres separated by a pitch of 305 µm and with a 250 µm diameter. The simulation is able to track the different energy deposition data (hits) within the phantom volume and store its interaction data.

5.3 Module Structure

To develop a better understanding of the Geant4 simulation and help facilitate the fibre differentiation work, an overview of the modular structure of the code was created, illustrated in Fig. 5.5.

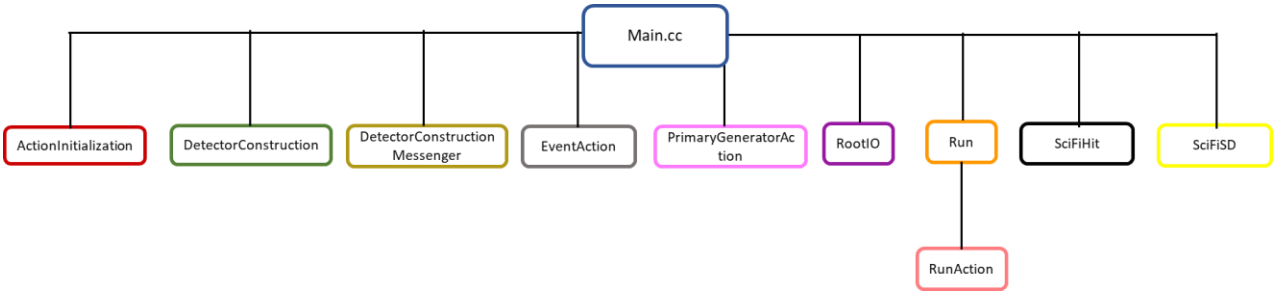

Fig. 5.5: A diagram outlining the structure of the ten modules in the original Geant4 simulation.

The original Geant4 code comprised of ten modules, each with a specific function:

- ActionInitialization: This module concerns the build and run actions used throughout the simulation. Any modifications to the action class must be defined in this module to avoid resorting to Geant4 default functions.
- DetectorConstruction: This module initializes all the parameters including scintillating fibre properties and geometry, phantom geometry, construction materials and the box geometry. It creates logical and physical volumes for the world, SmartPhantom, water, scintillating fibres, and the SciFi detector stations. It then creates sensitive detector regions (volumes where data can be recorded) which are later used to compile the energy deposition hit data. This module also defines the functions which allow the geometry and materials of the simulation to be modified.
- DetectorConstructionMessenger: This module defines the new modification UI commands relating to the functions in DetectorConstruction when parameters are modified.
- EventAction: This module manages what to do during an event and outputs the number of entries and the origin of the event. Using this information, it then writes to the output ROOT file, providing information about the hits.
- PrimaryGeneratorAction: This module defines the particle gun used to generate the incoming proton beam for the simulation. Using an input file, it generates the primary particles, assigning each with a pre-defined set of coordinates, momentum, and trajectory.
- RootIO: This module creates the output ROOT file and handles the storage of information that is constructed in the RunAction module. It creates a new TTree for every instance, with defined parameters: deposited energy, time of interaction, event number, the 3D coordinates of the event, step length and time between events.
- Run: This module manages the execution of the simulation in Geant4.
- RunAction: This module manages each run instance by instantiating RootIO to create a new output file and running PrimaryGeneratorAction. At the end of each run action, parameters are reset before the process is repeated.
- SciFiHit: This module defines where the hits in the sensitive detector volumes are stored.
- SciFiSD: This module defines and identifies each sensitive detector, initialising each with zero energy. It then initializes a hits collection – a container where the vectors of hits can be stored. The hits are processed and stored with the following information: sensitive detector of the hit, time of the hit, energy deposited, the step length, the 3D coordinates, time between events and the particle species.

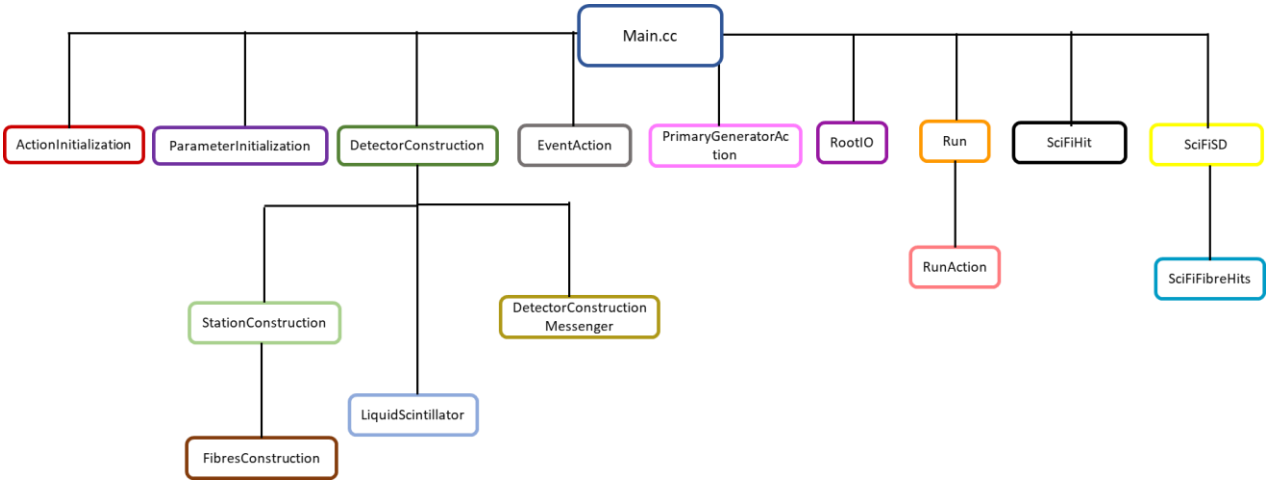

Fig. 5.6: A diagram showing the proposed amendments to the original module structure of the Geant4 simulation. The new structure incorporates five new modules to separate the existing code into distinct functions and improve its usability.

The code structure was not optimised which meant adapting and modifying the code was difficult. To improve this, a new modular structure was proposed to assign each module with a specific purpose and minimize the code in each module. The new modular diagram can be seen in Fig. 5.6.

The main alterations are as following:

- ParameterIntialization: This module will define all the parameters used in the other modules of the simulation. The centralized list of parameters will improve the functionality and accessibility of the simulation.
- DetectorConstruction: This module is modified to only initialize and modify the world and phantom properties.
- StationConstruction: This module is introduced to define and modify the detector station geometries.
- FibreConstruction: This module is proposed to define and modify the physical and logical volumes of the scintillating fibres.
- SciFiFibreHits: This module will classify the energy deposition hits into individual detectors and fibres. Further details on the method can be found in the following section.

The improved understanding of the simulation function gained from studying the code would assist the next software objective: localizing the energy deposition hits into fibres and detector planes.

5.4 Fibre Differentiation

The Geant4 simulation prior to project commencement did not localise energy deposition into each of the detectors and fibres. This meant that the data was unable to be used to reconstruct the Bragg peak using simulated detector measurements. Therefore, it was important to adapt the code to classify the energy deposition hits. To accomplish this, boundary conditions needed to be placed to define each fibre and detector location.

Each of the detectors were defined as set volumes confined to particular z-axis positions by which the coordinates of the energy deposition hits were filtered by: if they fell within these boundaries, they would be classified as being in the corresponding detector.

The fibre classification was then applied, where cylindrical volumes of 250 µm diameter and 305 µm pitch were used as the boundary conditions for each of the thirty-three fibres in each detector. For every individual hit classified as within a detector, they were either labelled into their corresponding fibre (numbered 1 to 33) or classified as a no hit (occurring when the energy deposition hit falls in the gap between consecutive fibres). The full method is illustrated by the diagram in Fig. 5.7.

These categories were then appended onto the details of each hit, producing a comprehensive list of energy deposition hits in each of the detectors.

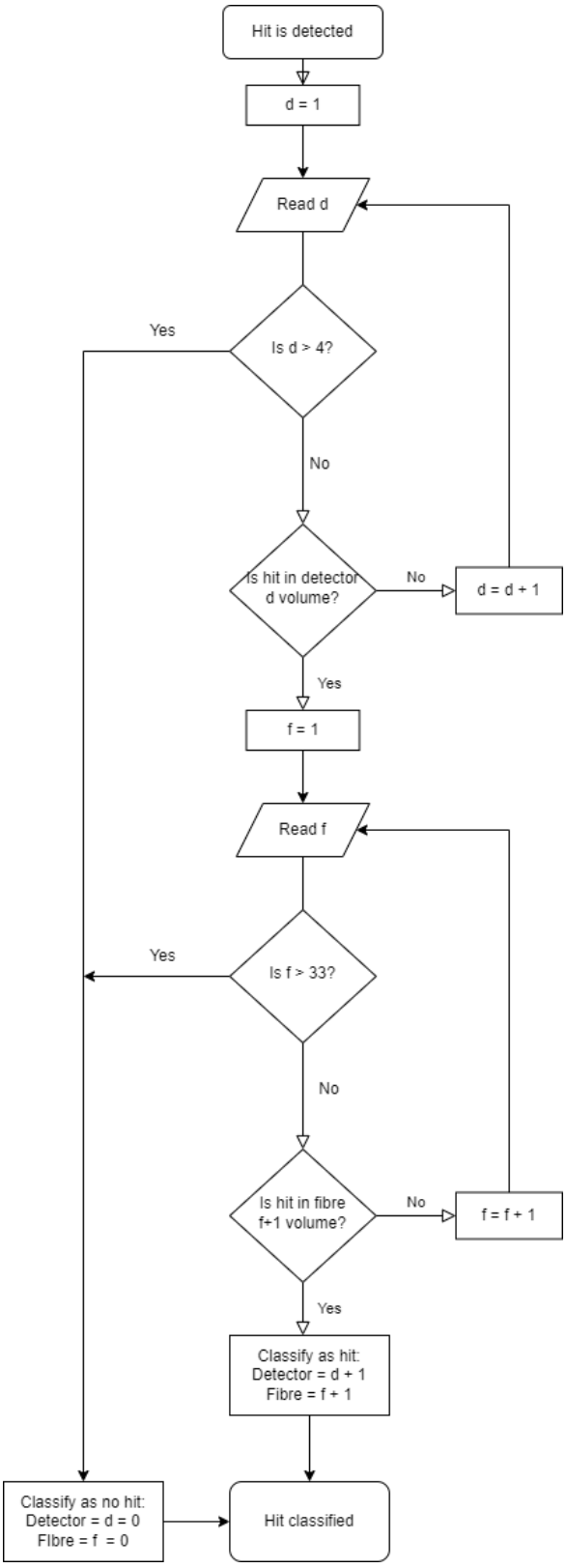

Fig. 5.7: A flow chart showing the fibre (*f*) and detector (*d*) classification process for the energy deposition hits.

5.5 Simulation Results

By analysing the simulation output data set, the total energy deposited in the individual fibres in each of the detectors can be determined as shown in Fig. 5.8. The graph shows that energy is consistently deposited within the central fibres, with a similar Gaussian distribution across the four detectors. The distributions for the detector fits follow the parameters shown in Table V. There is also an evident increase in energy deposition as the beam propagates further through the phantom.

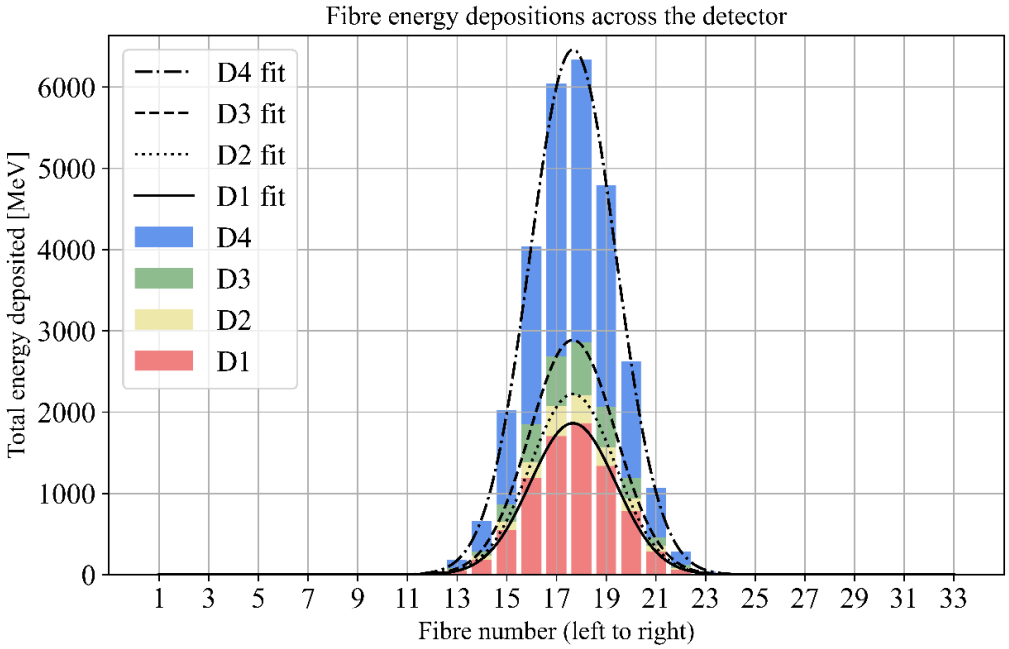

Fig. 5.8: Simulated energy deposition in each fibre in each detector with overlayed Gaussian fits showing a consistent energy deposition concentrated in the central fibres.

TABLE V
GAUSSIAN FIT PARAMETERS

Detector	σ	μ
1	1.712 ± 0.007	17.646 ± 0.007
2	1.712 ± 0.010	17.668 ± 0.010
3	1.680 ± 0.009	17.653 ± 0.009
4	1.692 ± 0.007	17.639 ± 0.007

The fibre depositions were then amalgamated to produce a total energy deposition value for each detector. Fig. 5.9 illustrates the simulated depth-dose distribution of the 20 MeV proton beam along the z axis of the phantom, with the total binned simulated energy deposition (in grey) and the energy deposited in each detector (in red). The errors are minute in comparison to the data points and stem from the simulation's output data variability. They were calculated using the standard deviation of the data points generated from different simulation data sets and are quoted in Table VI. An analytical Bortfeld fit was then applied to the detector deposition values (shown in dashed blue), with the aim of reconstructing the depth-dose curve (in dashed green). The reconstruction accuracy was verified using Kolmogorov-Smirnov (K-S) and R^2 tests, where the correlation was calculated to be 98.3% and 0.892, respectively. The simulation results are limited by the binning used for the data (250 μm to match the fibre diameters) as energy deposition locations are lost within the bins themselves. However, despite this, the high accuracy attests to the validity of the project and its aims: using four SciFi detector measurements, in simulation, yields an accurate beam profile reconstruction.

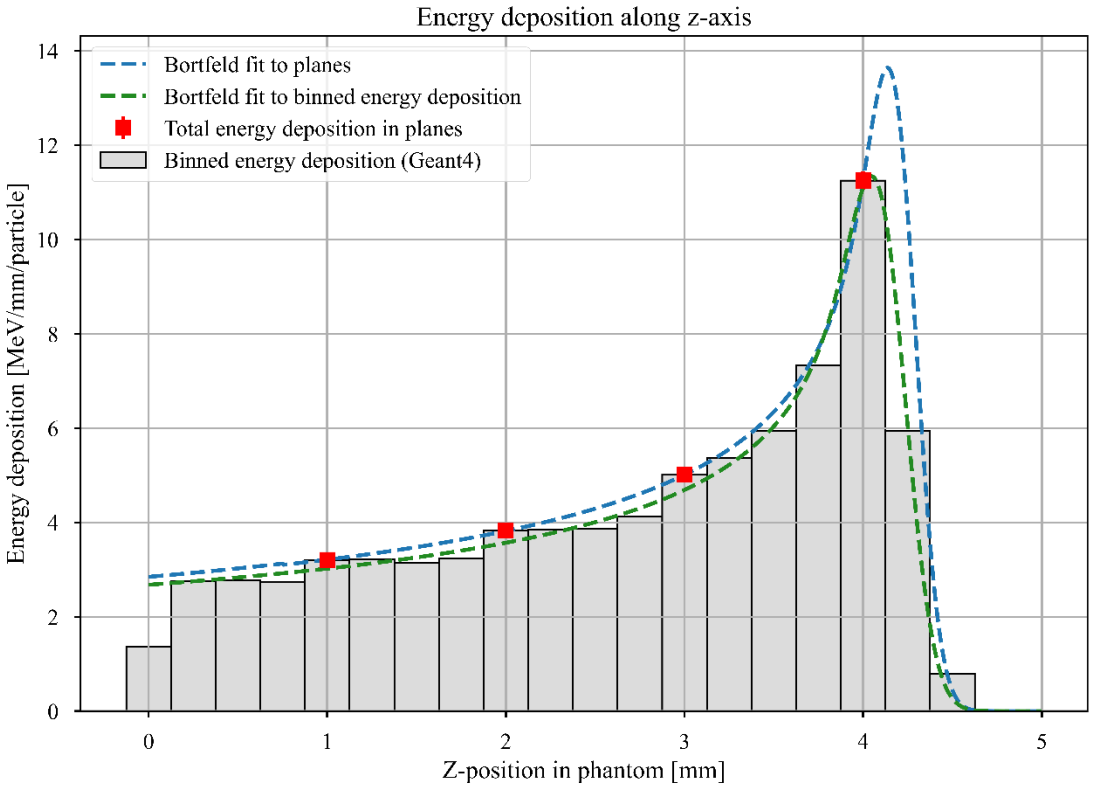

Fig. 5.9: Simulated binned proton beam energy deposition in SciFi detectors (grey) with the associated depth-dose curve (green). An analytical fit [18] (blue) to detector measurements (red) reveals the Bragg peak. This reconstruction accuracy was determined to be 98.3% and 0.892 using the Kolmogorov-Smirnov (K-S) and R^2 tests respectively.

TABLE VI
SIMULATION ERRORS ON DETECTOR DEPOSITION VALUES

Detector	Error
1	0.674
2	0.547
3	1.052
4	1.606

To verify the simulation accuracy with experimental data, the reconstructed Bragg peak location was compared to two sources: the NIST data for a 20 MeV beam and values generated by the GATE Monte Carlo simulation [45]. Fig. 5.10 shows the NIST and simulation range values for a 20 MeV proton beam to be (4.260 ± 0.018) and (4.2420 ± 0.0818) mm respectively [45]. Comparing these values to the reconstructed Bragg peak location at 4.139 mm, accuracy is determined to be 97.2% and 97.6% respectively. This high accuracy affirms that the simulation functions precisely to model the 20 MeV proton beam.

Energy (MeV)	Statistical uncertainty in measuring R_{73} (mm)	R_{73} (mm)	NIST R_{CSDA}[a] (mm)	Delta R measured[b] (mm)
5	8·9140*E*−02	3·77000*E*−01	3·623*E*−01	−1·470*E*−02
10	8·5370*E*−02	1·19800*E*+00	1·230*E*+00	3·200*E*−02
15	7·6720*E*−02	2·50800*E*+00	2·539*E*+00	3·100*E*−02
20	8·1810*E*−02	4·24200*E*+00	4·260*E*+00	1·800*E*−02
25	7·0750*E*−02	6·35300*E*+00	6·370*E*+00	1·700*E*−02
30	8·2750*E*−02	8·84000*E*+00	8·853*E*+00	1·300*E*−02
40	6·1500*E*−02	1·48690*E*+01	1·489*E*+01	2·100*E*−02

Fig. 5.10: Snippet of table taken from [45] showing the proton beam ranges and errors for various energies with the R_{73} value being generated by a GATE Monte Carlo simulation and the R_{CSDA} taken from the NIST database [46].

The next step was to investigate different detector configurations to evaluate the impact of detector location on the simulation's reconstruction accuracy. Table VII depicts five detector configurations which were assessed, alongside their corresponding K-S and R^2 test values. Results that placed the fourth detector after the Bragg peak were unable to return Bortfeld fits. Based on these results, the optimal configuration would have the fourth detector located as close to the Bragg peak as possible on its rising edge, evidenced by the results of configuration five which yielded high accuracy values of 98.3% and 0.988.

TABLE VII
ACCURACY OF RECONSTRUCTIONS FOR DIFFERENT DETECTOR CONFIGURATIONS

Configuration	Detector 1 Distance / mm	Detector 2 Distance / mm	Detector 3 Distance / mm	Detector 4 Distance / mm	K-S Test	R^2 test
1	1	2	3	4	98.3%	0.892
2	1	2	3	4.5	N/A[1]	N/A[1]
3	1	2	3	3.5	83.2%	0.853
4	1	2	3	4.25	N/A[1]	N/A[1]
5	1	2	3	3.75	98.3%	0.988

[1] These configurations did not return a Bortfeld fit and so no test values were generated.

5.6 Future Considerations

The next steps to further improve the simulation and reconstruction of the proton beam depth-dose distribution are:

- To implement the discussed modular changes for improved efficiency, functionality, and usability of the simulation code.
- To investigate the use of a quenched Bragg curve fit which may improve the accuracy of the reconstruction by combining Birk's law and Bortfeld's curve to correct for quenching effects caused by the increased linear energy transfer within the scintillating fibres [35].
- To explore the limitations of the simulation Bragg peak reconstruction when using a different number of detectors and testing more detector configurations. Assessing the impact of detector location on the reconstruction informs optimal detector configuration for the SmartPhantom which will advise future practical applications.
- To improve the correspondence of the simulation to practical experiment. Further components need to be simulated including the scintillating fibre cladding, clear fibre connection and camera. By implementing these, the simulation results will become more comparable to the experimental data.

Chapter 6

Experimental

This chapter details the design and manufacturing process of the SciFi detector prototypes alongside the testing and evaluation methods.

6.1 Objectives

The main objective was to design and build a SciFi detector prototype capable of accurately measuring the energy deposition of a proton beam. The design will be evaluated against four key criteria:

1. Feasibility – The ease and accessibility of construction process including time, cost and labour involved.
2. Reproducibility – The consistency in uniform detector manufacturing.
3. Precision – The scintillating fibre alignment across the detector plane.
4. Accuracy – The pitch distance of the scintillating fibres.

The prototype must also be assessed to determine its performance and image processing software must be developed to map the detector output.

6.2 Mark I

Previous work on the SmartPhantom influenced key design elements of the project's mark I prototype.

6.2.1 Initial Design Considerations

The preliminary investigation involved reviewing the design considerations proposed by prior work. The key recommendations were to revise the frame design to ensure appropriate and functional structure, to ensure the adhesive used in the manufacturing process did not affect fibre performance, to preserve quality of readout by reducing scintillating fibre exposure to the external environment, and to maximise readout by ensuring perfect alignment of the clear and scintillating fibres. These recommendations were addressed by the following: the plastic frame was designed to include thin metal supportive plates to maintain structure, the frames incorporated a well design to contain and reduce adhesive run-off, and the scintillating and clear fibre connection was moved into the frame itself to avoid external light sources and ensure alignment between both fibres.

After careful assessment of the previous designs, there were also three notable issues that required further consideration:

- Size: The previous iterations of frame design were large (15 x 15 cm^2) especially in comparison to the small beam size. This meant that the incident beam interacted with a small area of the detector, rendering the rest of the detector's active area redundant. This corresponds to wasted scintillating fibre, an expensive resource.
- Uniform tension: There were also issues with ensuring that the fibres were taut throughout the frame. This was particularly important in maintaining the quality and uniformity of the light yield across the detector plane.
- Perfect alignment: Due to the small diameter of the scintillating fibre (250 µm), ensuring perfect alignment across the entire frame is difficult as the fibres are indiscernible by eye. Avoiding fibre cross over and achieving perfect alignment is important to preserve the location of the energy deposition hit.

To address these key issues, the following solutions were implemented: the active area of the detector was reduced to 1 cm^2 to minimize scintillating fibre usage, a mixture of epoxy resin and applied tension were used to ensure uniform tension and the frame design incorporated the use of holes to preserve fibre spacing and alignment in the frame.

6.2.2 Manufacturing and Assessment

To address the previous issues, a new frame design was created. The assembly of the initial design included threading the thirty-three scintillating fibres through the 290 µm holes drilled on each side of the frame before connecting each side to a vacuum pump using a specially manufactured attachment piece. The epoxy resin would then be injected into the well-cavities and the resin would

be pulled through the holes using the vacuum pump, fixing the fibres in place, and eliminating any air pockets which may attenuate the photon output.

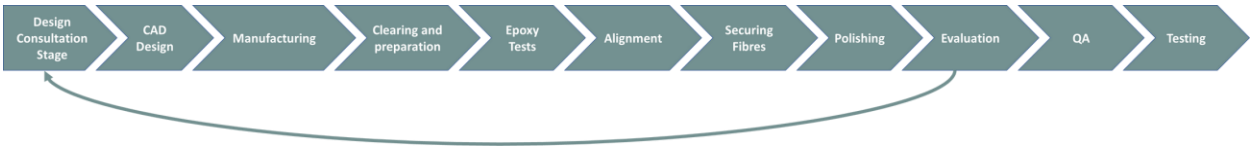

Fig. 6.1: Flowchart showing the key stages of the construction process.

However, during the construction phase (depicted in Fig. 6.1), many issues emerged with this prototype design. The small 290 µm holes needed specialist drill heads and due to the precise 305 µm pitch spacing required, this process took a long time to complete. Once manufactured, the frames, which were made from plastic, required cleaning and the holes needed to be deburred to remove plastic debris. The deburring process spanned many weeks and was difficult due to the small size and incomplete clearance of the holes. As such, it was eventually decided that the deburring process was not feasible. To resolve this, the top halves of the frames were sanded to turn the holes into grooves as shown in Fig. 6.2. This process would create two frame halves, each with grooves, between which the scintillating fibres could be sandwiched. These grooves were then cleared of debris and following this, the fibres were individually aligned onto the frame, using the grooves as guides to preserve alignment and spacing. After the alignment of the fibres, epoxy resin was applied to the well-cavities. The previous idea to utilize a vacuum pump was discarded as it was quickly found that the vacuumed pressure pulled the fibres out of alignment. After the epoxy resin was set, the frame was polished and cleaned.

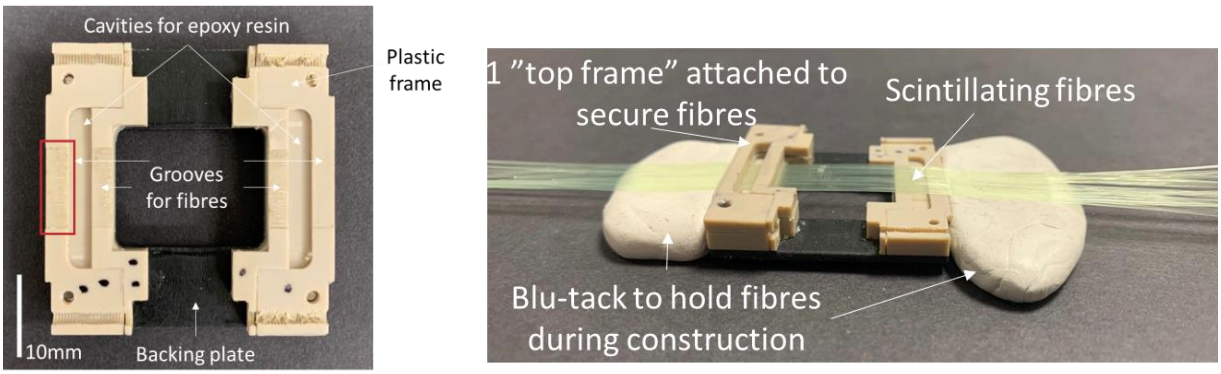

Fig. 6.2: Images of the mark I prototype under construction. Frame with grooves after the sanding and cleaning stages (left). Constructed frame before epoxy resin application (right).

Though the mark I prototype was manufactured, there were many associated issues. The scintillating fibre alignment was poor due to the difficulty in discerning the individual grooves by eye and the absence of constant tension correlated to issues with securing the fibres into the correct grooves. There were also problems with the epoxy resin mixture as the recommended 3:10 epoxy to hardener ratio had a 24-hour setting time, with fibre alignment not being secured until the epoxy sets. These issues resulted in the mark I prototype having vast alignment errors and being unsuitable for accurately measuring dose. When assessed against the four initial criteria, the mark I prototype was deemed unsuccessful:

1. Feasibility – The construction process was time and labour intensive, making it a non-functional and inaccessible design.
2. Reproducibility – The difficult, single-detector manufacturing process makes reproducibility low.
3. Precision – The alignment error and fibre cross-over erode the output precision.
4. Accuracy – The fibre alignment and pitch are very inconsistent, leading to low detector accuracy.

6.3 Mark II

The mark I prototype was used to inform modifications which were incorporated into the mark II design.

6.3.1 Design Considerations

The next step was to design a new prototype that addressed the challenges faced by the mark I. The predominant issue of the previous iteration was the difficulty in ensuring alignment and constant tension stemming from the intricacy of securing individual fibres into indiscernible grooves. To resolve this, the re-introduction of the winding jig was proposed. The winding jig, depicted in Fig. 6.3, was an alignment method used in previous iterations, which involved wrapping the scintillating fibre around a jig, with the pitch spacing controlled by pre-cut grooves in the PTFE lobes. By using the winding method, constant tension could be applied to the fibres, ensuring they remained secure and fixed in alignment throughout the construction process. However, the previous winding jig was very large compared to the proposed 1 cm^2 active area detectors, which would lead to high fibre waste. Consequently, the winding jig had to be altered to fit the smaller detectors by resizing the main frame.

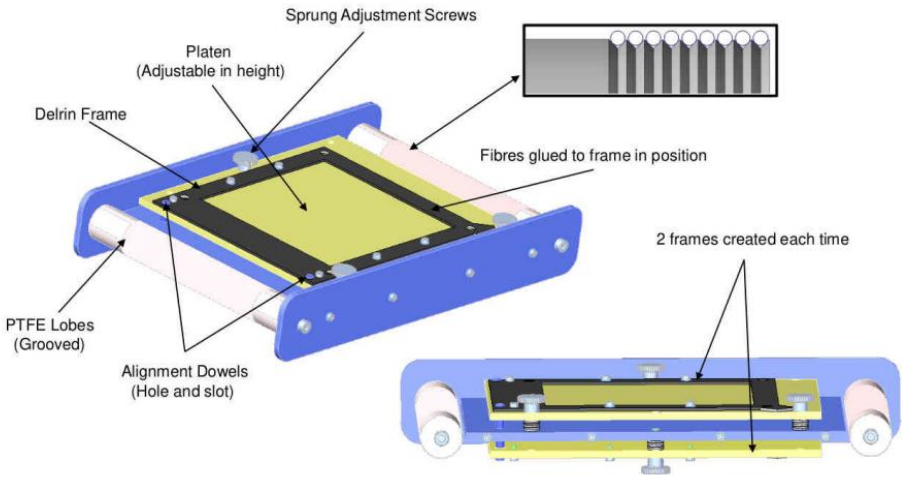

Fig. 6.3: Schematic of the previously used winding jig designed to wind and align the SciFi frames taken from [10].

Fig. 6.4 illustrates the modified winding jig, which is capable of manufacturing four detector planes (two on either side) simultaneously - a stark improvement on design feasibility. The sandwiched frame design was retained. As the inbuilt grooves in the winding jig maintained fibre alignment, the frames were redesigned to use cavities to embed the scintillating fibres, reducing manufacturing time as precise holes and grooves were not required. The frame material was also altered from plastic to aluminium to provide a stronger frame and avoid plastic debris. The use of the winding jig to maintain tension also negated the requirement of an epoxy resin cavity as only a very thin layer of adhesive was needed to secure the fibres. The newly proposed mark II prototype would offer improved fibre alignment and tautness, quicker manufacturing times and simultaneous detector creation.

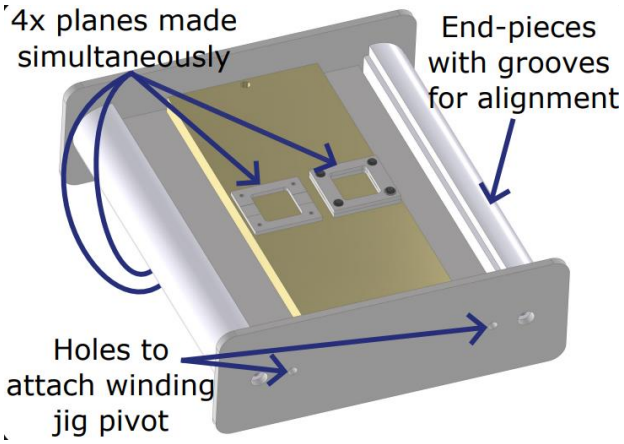

Fig. 6.4: Schematic of the modified and resized winding jig with the new aluminium frame design attached.

6.3.2 Manufacturing and Assessment

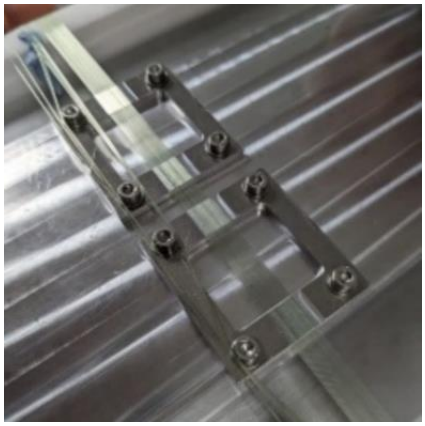

Fig. 6.5: Image of the mark II prototype under construction where the scintillating fibres are being aligned using the winding jig.

Compared to the mark I prototype, the manufacturing process for the winding jig and frames was much quicker, spanning only a few weeks. To assemble the frames, the scintillating fibre was wound thirty-two times about the winding jig, ensuring that they sat in the cavity of the frame halves each time as depicted in Fig. 6.5. The winding alignment process was quicker and easier due to the inbuilt grooves structuring the fibre spacing, enabling four detectors to be constructed in less than half a day. After alignment, the fibres were secured using a thin layer of epoxy resin brushed onto the fibres trapped in the cavity. When the fibres were fixed and set, the tops of the frames were secured, and the frames were removed from the winding jig as shown in Fig. 6.6. The frames were then polished and cleaned.

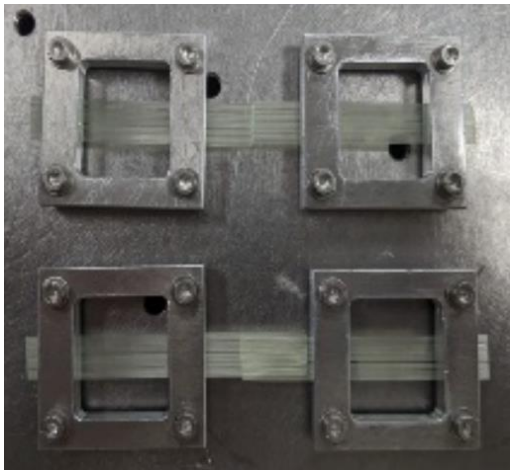

Fig. 6.6: Image of the constructed mark II prototype post alignment and ready to be polished and cleaned.

Though the mark II prototype was vastly improved compared to the mark I, with more precise and consistent fibre spacing and accuracy, there were some issues that remained. Primarily, a large amount of scintillating fibre was wasted in the winding process, stemming from the empty space in the winding jig which can be seen in Fig. 6.5. To remedy this, a more effective use of the winding jig area could be employed to manufacture more detectors at a time (i.e. six instead of four). Due to the use of a cavity in the frame design, there was also difficulty in keeping the fibre pitch consistent especially when applying the epoxy resin. The weight of the epoxy resin caused the fibres to be pushed out of alignment as they were not supported in place by any structure. This issue could be addressed by reintroducing the grooves into the frame design to ensure alignment is maintained. Lastly, the aluminium frames were susceptible to high levels of reflection which could impact later testing stages. This could be resolved by oxidising the metal or using an alternative material such as carbon fibre.

Overall, the mark II prototype was deemed successful when assessed against the four criteria previously described:

1. Feasibility – The construction process was quick and required minimal labour.
2. Reproducibility – There is a high level of consistency in the construction process due to the simultaneous detector production.
3. Precision – The scintillating fibres were predominantly taut and aligned throughout the frame, with no fibre cross over.
4. Accuracy – The alignment and pitch distance of the scintillating fibres was relatively consistent; however, this could be improved by the reintroduction of grooves into the frame design.

6.4 Testing

Following the successful creation of the mark II prototype, the design was required to undergo quality assurance procedures to quantify the detector performance. In particular, the objectives of the testing stage were as following:

- To perform a counting and ordering check to assess correct fibre placement with no cross over.
- To determine pitch distance between the scintillating fibres to quantify detector accuracy.
- To evaluate the energy deposition across the fibres in the detector.
- To evaluate the energy deposition in the detector with increasing distance (z-direction) from detector to source.

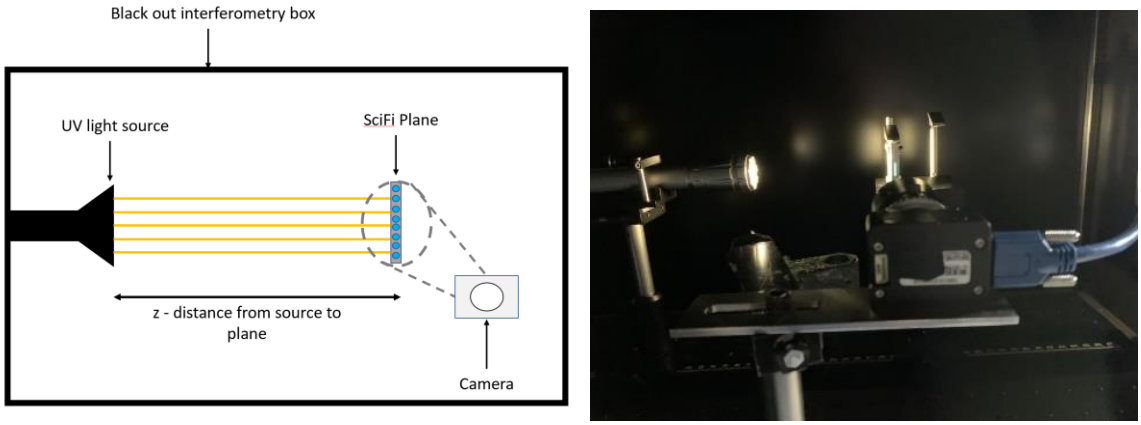

Fig. 6.7: Diagram of the testing apparatus including the ultraviolet light source, detector, and camera (left). Image of the real testing apparatus inside an interferometry box (right).

To perform these tests, the apparatus and equipment was set up as shown in Fig. 6.7. These assessments required a blacked-out area to avoid external light sources affecting the quality of the scintillating fibre light yield. This was achieved by using an interferometry box which had the ability to eliminate external light and keep the set up stable and secure. The experiment used an ultraviolet torch to illuminate the SciFi detector which would be placed at a specific z-distance away from the light source. A camera was then set up to capture the output of the scintillating fibre ends which would illuminate when energy was deposited. An example of the detector output (camera readout) is shown in Fig. 6.8.

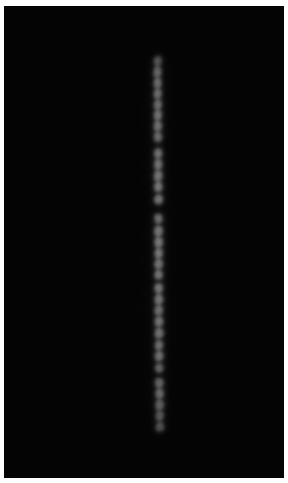

Fig. 6.8: Image of the camera output of the scintillating fibre readout after illumination. This image is taken at z = (1 ± 0.1) cm.

The first test conducted was the counting and ordering check. To achieve this, a precise 250 µm pinhole cover was attached to the ultraviolet torch to concentrate the beam. The beam was then shone down each of the fibres individually from top to bottom to verify that there was no fibre cross-over. Fig. 6.9 shows five example consecutive frames depicting the upwards moving beam correlating to a synchronously moving output. This test concluded that there was no cross over, with the scintillating fibres being perfectly aligned across the frame.

Fig. 6.9: Examples of five frames used in the counting and ordering check where the ultraviolet light source is shone down each individual fibre to check the corresponding output. The light output can be seen to be moving upwards.

The following assessment was conducted to evaluate the last three objectives: determining pitch, energy deposition in the individual fibres and detector energy deposition across a varying distance. The SciFi detector was first placed at (0.5 ± 0.1) cm from the ultraviolet light source and the detector output was captured. The camera was set to capture the output across five frames to account for the pulsing illumination of the ultraviolet torch. This was then repeated at (1.0 ± 0.1) to (11.0 ± 0.1) cm in intervals of 1 cm. Once the data was gathered, the next step was to process the images.

6.4.1 Image Processing Software

Software was developed to map the camera output to the individual scintillating fibres. The image processing software (depicted in Fig. 6.10) operates in a series of steps:

1. The software first loads the camera output and converts the image to greyscale.
2. A threshold value is calculated and applied as a mask to isolate the fibres and minimize any background effects including glare and external light sources.
3. The converted image is then passed through a function that identifies and stores the individual fibres. The process of identifying the fibres utilises Hough transforms to detect each of the fibre output circles.
4. For each of the detected fibres, the centre of mass coordinates are calculated and stored as the location of the fibre.
5. The corresponding pixel intensity of the fibre at its centre of mass is then identified and stored as the fibre output signal.

6. The data is finally amalgamated for the whole image to produce an array with the identified fibres, coordinates, and pixel intensity values.

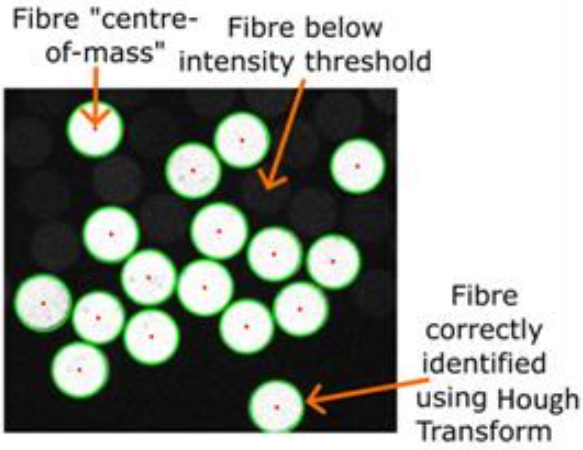

Fig. 6.10: Example of illuminated scintillating fibre ends under image processing code. The image used to test the software was taken from [10].

This software was employed to process the images obtained in the testing stages. Using the collated data, the pitch distance could be obtained by calculating the distances between the coordinates of each of the fibres. The energy depositions (i.e. pixel intensities) in each of the fibres in the detector at different z-distances could also be obtained and by using these results, the total energy deposited in the detector (the sum of all fibre depositions) could be calculated.

6.5 Experimental Results

It was important to first quantify the image processing software accuracy. The detection accuracy was calculated as the percentage of fibres correctly identified by the software out of the total number of existing fibres. The software accuracy across a range of distances can be seen in Table VIII. Though the detection accuracies across all the distances were high (above 90%), at closer distances there is an evident increase in accuracy. The overall results indicate that the software is relatively accurate up to a distance of around 5 cm, beyond which accuracy starts to decrease. It is important to further improve the detection percentage by altering the parameters of the Hough transform to ensure all fibres are being accurately identified.

TABLE VIII
FIBRE DETECTION ACCURACY OF IMAGE PROCESSING SOFTWARE

Distance / cm	Detection Percentage
0.5	95.76%
1.0	95.76%
2.0	95.15%
3.0	95.15%
4.0	95.15%
5.0	92.73%
6.0	92.12%
7.0	93.94%
8.0	93.94%
9.0	91.52%
10.0	92.12%
11.0	95.15%

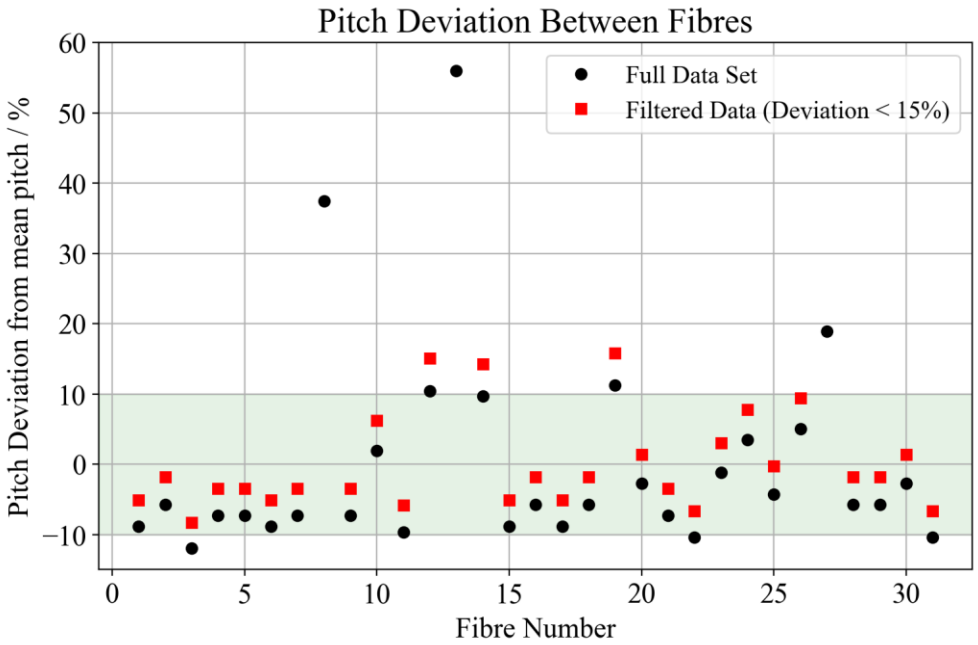

Fig. 6.11: Percentage pitch deviation from the average pitch value across the detector (black) - 74.2% of the deviations fall within 10% of the average pitch. When filtered for anomalies (defined as data points with deviations over 15%), 89.3% of the deviations fall within 10% of the new average pitch (red).

The pitch accuracy was determined to be 74.2%, with an accurate pitch being defined as being within 10% of the average pitch value. As illustrated in Fig. 6.11, there were three major pitch anomalies (where the deviation > 15%) which were due to the difficulties with securing the fibres in place during construction. When these were filtered out, the pitch accuracy improved to 89.3%. This will need to be further improved to ensure that the localisation of the energy deposition within the fibres is accurate, as the pitch directly corresponds to the detector accuracy.

Fig. 6.12 depicts the fibre energy deposition at two distances (1 and 11 cm) across the detector. The errors on the pixel intensity originate from the fluctuating ultraviolet light source intensity. To account for this, the average value over a series of frames was used and the error was calculated from the standard deviation across the frames. The results indicate that at a closer distance of 1 cm, the beam is concentrated on the central fibres as the pixel intensity drops off rapidly towards the end fibres. In contrast, at a further distance of 11 cm, there is a more consistent pixel intensity across the fibres in the detector as shown by the much flatter distribution. This behaviour stems from the beam's small width – at close distances, the beam is only able to directly illuminate the central fibres but as the distance increases, its illumination area increases.

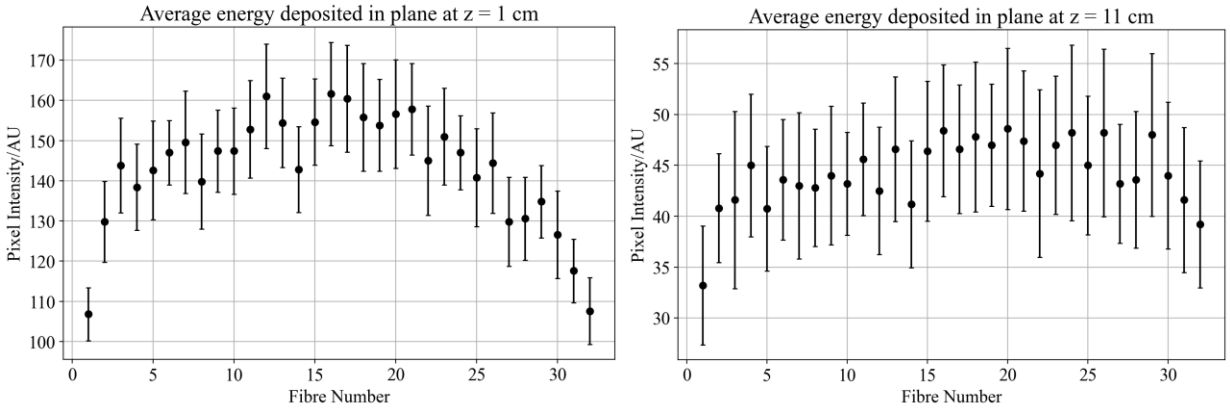

Fig. 6.12: Fibre-Energy distribution across the detector at 1cm (left) and 11cm (right) showing a more central concentrated beam at 1cm and a flatter distribution at 11cm.

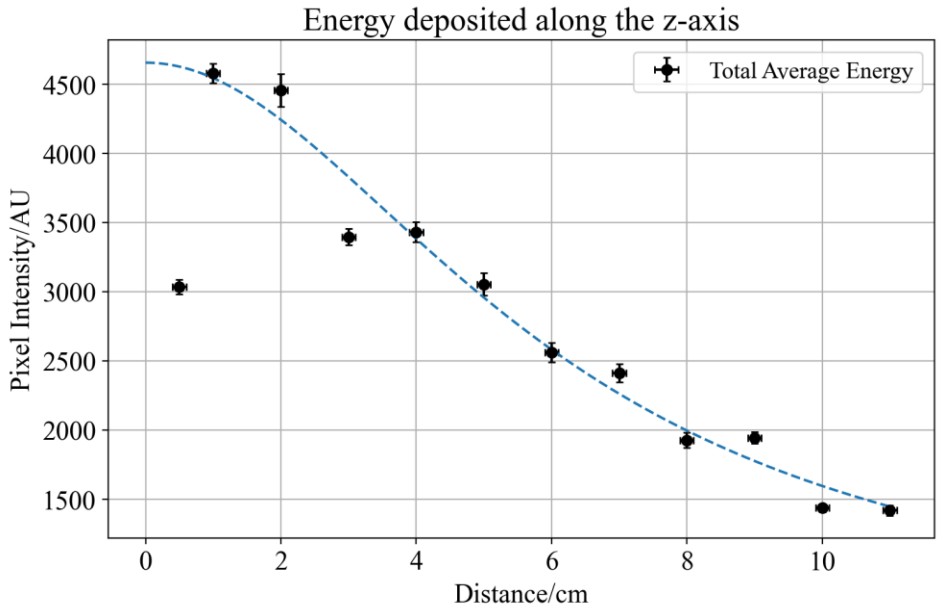

Fig. 6.13: Energy deposition along the z-axis for the ultraviolet light source showing a rising edge before a rapid decline, with an empirical fit shown in blue.

The pixel intensity at various z-distances was examined, with the graph illustrated in Fig. 6.13. The graph shows a rising edge until 1 cm, stemming from the beam's restricted illumination area, before a large decline as the detected pixel intensity falls with increasing distance. This decline is expected as the UV source signal weakens as it travels a further distance. The graph shows an empirical fit of

$$y = \frac{A}{x^2 + B} + C, \quad (6.1)$$

where A, B and C are arbitrary constants. As expected, for large distances (for $x \gg B$), this tends to the inverse square law.

The errors in pixel intensity are due to the fluctuating UV beam which translates to a high range in pixel intensity values. This uncertainty impacts the investigation as the results become less comparable between frames and distances. To remedy this, the frame rate must match the UV source intensity variation rate which can be achieved by measuring the light output of the source across a set length of time and calculating the pulse-to-pulse period. This can be used to set the camera frame capture time.

6.6 Future Considerations

Many modifications can be implemented to further improve the prototype design and performance:

- A second perpendicular layer of aligned fibre is required to localise the energy deposition in the detector in two dimensions.
- To improve the alignment and pitch accuracy of the fibres, grooves could be reintroduced to the design.
- The frame material needs to be revised to avoid beam reflections.
- A connection for the scintillating to clear fibres is needed to avoid the scintillating fibre exposure to external light sources. The alignment of the scintillating and clear fibres is very important to preserve the quality of light yield. This can be addressed by using a design for an alignment jig such as one shown in Fig. 6.14. Once the connection is established, the clear fibre must be potted to preserve the light yield.
- The prototype must be tested with a proton beam source to evaluate its Bragg peak reconstruction accuracy.

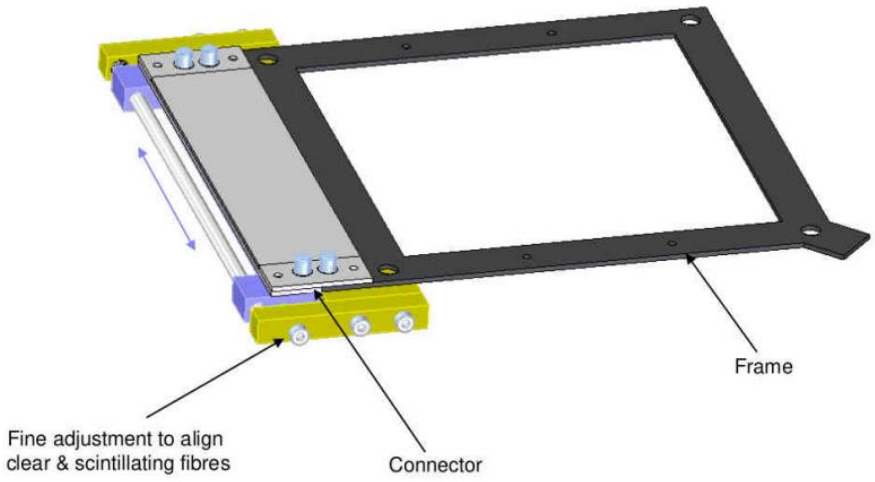

Fig. 6.14: Schematic of the previously used alignment jig designed to connect the scintillating and clear fibres taken from [10].

Chapter 7

Conclusion and Final Remarks

This project presented a Geant4 simulation of a 20 MeV proton beam which generated simulated results for the energy deposition in the SciFi detector, used to successfully reconstruct the depth-dose distribution. The concept and developments for the SciFi detector were outlined, with two prototypes being developed and the mark II undergoing quality assurance testing using an ultraviolet light source.

7.1 Geant4 Simulation

The main software objective was to expand a pre-existing Geant4 simulation to localise a 20 MeV proton beam dose deposition within the SciFi detectors and fibres. Having successfully expanded the code, the data was used to reconstruct the simulated depth-dose distribution solely using the energy deposition values in the four detector planes. The resulting reconstruction obtained correlation accuracies of 98.3% and 0.892 when evaluated using the K-S and R^2 tests. The reconstructed Bragg peak at 4.139 mm was also found to be 97.2% accurate compared to NIST data. The optimal configuration for the detectors was found to be placing the fourth detector close to the Bragg peak and on its rising edge. The next steps to further advance the simulation would be to implement the new modular modifications suggested to improve code efficiency and usability, to investigate the quenched Bragg curve fit as an analytical approximation and to further investigate different detector numbers and configurations. To improve the simulation comparability to the experimental data, further features must be added to the simulation including the scintillating fibre cladding, clear fibre connection and camera.

7.2 SciFi Detector Design

The principal aim of the project was to design and construct a prototype for the SciFi detector, capable of accurately measuring energy deposition. This prototype was evaluated against four main criteria (feasibility, reproducibility, precision, and accuracy) before being assessed to quantify the detector performance. Two prototype designs were created: Mark I was judged unsuccessful due to extremely poor fibre alignment and a difficult manufacturing process whilst mark II was considered successful with improved alignment and precision. The mark II prototype scintillating fibre pitch accuracy was found to be 74.2%. To further improve the design, steps would include introducing a second perpendicular fibre layer for 2D energy localisation, the reintroduction of grooves into the design to maintain pitch and alignment, the revision of frame material to avoid beam reflections and the design of a scintillating to clear fibre connection. Finally, the design would need to be evaluated using a proton source to assess its depth-dose distribution reconstruction accuracy for PBT use.

7.3 Final Remarks

To conclude, this project has demonstrated the importance of PBT and accurate dosimetry. The SciFi detector is a very promising dosimeter, capable of providing real-time 3D beam profile measurements. To further the development of the SciFi detector, there are some important future considerations. Firstly, the design must be evaluated for its intended use within the SmartPhantom and as part of the LhARA project. The LhARA project proposes the use of the SmartPhantom alongside ion-acoustics – a promising dosimetric technique that measures the thermoacoustic pressure waves generated when ionising radiation energy is deposited. However, the presence of SciFi detectors in the SmartPhantom causes acoustic reflections which impacts the thermoacoustic signal. A potential solution would be to investigate the use of liquid scintillator in the SmartPhantom, which would not have an impact on the acoustic signal, and potentially could be calibrated using the SciFi detectors. As the global demand for cancer treatment rises, the development of PBT and novel dosimetry techniques becomes increasingly important. This project demonstrates progress towards the development of a reliable SciFi detector, which could improve the accuracy and efficiency of PBT treatment.

Bibliography

[1] World Health Organization, “Cancer,” 03 02 2022. [Online]. Available: who.int/news-room/fact-sheets/detail/cancer. [Accessed 25 09 2022].

[2] J. Ferlay, M. Colombet, I. Soerjomataram, D. M. Parkin, M. Piñeros, A. Znaor and F. Bray, “Cancer statistics for the year 2020: An overview,” *International journal of cancer,* 2021.

[3] B. Rachet, l. Ellis, C. Maringe, T. Chu, U. Nur, M. Quaresma, A. Shah, S. Walters, L. Woods, D. Forman and M. Coleman, “Socioeconomic inequalities in cancer survival in England after the NHS cancer plan,” *Br J Cancer,* vol. 103, no. 4, pp. 446-53, 2010.

[4] G. Singh and A. Jemal, “Socioeconomic and Racial/Ethnic Disparities in Cancer Mortality, Incidence, and Survival in the United States, 1950-2014: Over Six Decades of Changing Patterns and Widening Inequalities.,” *Journal of environmental and public health,* 2017.

[5] R. Baskar, K. A. Lee, R. Yeo and K. W. Yeoh, “Cancer and radiation therapy: current advances and future directions,” *International journal of medical sciences,* vol. 9, no. 3, pp. 193-199, 2012.

[6] E. T. Vitti and J. L. Parsons, “The Radiobiological Effects of Proton Beam Therapy: Impact on DNA Damage and Repair,” *Cancers,* vol. 11, no. 7, p. 946, 2019.

[7] J. Thariat, S. Valable, C. Laurent, S. Haghdoost, E. Pérès and M. Bernaudin et al., “Hadrontherapy Interactions in Molecular and Cellular Biology,” *International journal of molecular sciences,* vol. 21, no. 133, 2019.

[8] W. D. Newhauser and R. Zhang, “The physics of proton therapy Physics in Medicine and Biology,” *Physics in Medicine and Biology,* vol. 60, 2015.

[9] S. H. Park and J. O. Kang, “Basics of particle therapy I: physics,” *Radiation oncology journal,* vol. 29, no. 3, pp. 135-146, 2011.

[10] H. Lau, “Medical Applications for Particle Physics,” Imperial College London, 2022.

[11] R. R. Wilson, “Radiological Use of Fast Protons,” *Radiology,* vol. 47, no. 5, pp. 497-491, 1946.

[12] H. A. Bethe, “Molière’s Theory of Multiple Scattering,” *Physical Review,* 1953.

[13] U. Fano, “Inelastic Collisions and the Molière Theory of Multiple Scattering,” *Physical Review,* vol. 93, p. 117–120, 1954.

[14] S. Braccini, "Scientific and Technological Development of Hadrontherapy," *Astroparticle, Particle and Space Physics, Detectors and Medical Physics Applications.,* pp. 598-609, 2010.

[15] A. M. Kellerer, K. Hahn and H. H. Rossi, "Intermediate dosimetric quantities," *Radiation research,* vol. 130, no. 1, p. 15–25, 1992.

[16] D. R. Grimes, D. R. Warren and M. Partridge, "An approximate analytical solution of the Bethe equation for charged particles in the radiotherapeutic energy range.," *Scientific reports,* vol. 7, no. 1, 2017.

[17] AVO, "Be part of the future of cancer treatment," [Online]. Available: http://www.avoplc.com/en-gb/LIGHT/ThePotential-of-Proton-Therapy . [Accessed 22 02 2023].

[18] T. Bortfeld, " An analytical approximation of the Bragg curve for therapeutic proton beams.," *Medical physics,* vol. 24, no. 12, p. 2024–2033, 1997.

[19] G. Kraft, "Tumor therapy with heavy charged particles," *Progress in Particle and Nuclear Physics,* pp. 473-544, 2000.

[20] S. Ray, E. Cekanaviciute, I. P. Lima, B. S. Sørensen and S. V. Costes, " Comparing Photon and Charged Particle Therapy Using DNA Damage Biomarkers.," *International journal of particle therapy,* vol. 5, no. 1, pp. 15-24, 2018.

[21] K. C. Jones, C. M. . Seghal and S. Avery, "Proton beam characterization by proton-induced acoustic emission: simulation studies," *Physics in Medicine & Biology,* vol. 61, no. 6, 2016.

[22] F. M. Khan, The physics of radiation therapy: third edition, Lippincott Williams & Wilkins, 2003.

[23] X. Tian, K. Liu, Y. Hou, J. Cheng and J. Zhang, "The evolution of proton beam therapy: Current and future status," *Molecular and clinical oncology,* vol. 8, no. 1, pp. 15-21, 2018.

[24] H. Paganetti and T. Bortfeld, "'Proton beam radiotherapy - the state of the art," *New Technologies in Radiation Oncology,* pp. 1-36, 2005.

[25] H. Paganetti, Proton Beam Therapy, IOP Publishing Ltd , 2017.

[26] M. Lodge, M. Pijls-Johannesma, L. Stirk, A. Munro, D. De Ruysscher and T. Jefferson, "A systematic literature review of the clinical and cost-effectiveness of hadron therapy in cancer," *Radiotherapy and Oncology,* vol. 83, no. 2, 2007.

[27] B. Jones, S. J. McMahon and K. M. Prise, "The Radiobiology of Proton Therapy: Challenges and Opportunities Around Relative Biological Effectiveness," *Clinical oncology (Royal College of Radiologists (Great Britain)),* vol. 30, no. 5, 2018.

[28] M. Kramer, O. Jakel, T. Haberer, G. Kraft, D. Schardt and U. Weber, "Treatment planning for heavy-ion radiotherapy: physical beam model and dose optimization," *Physics in Medicine and Biology,* p. 3299–3317, 2000.

[29] A. Kurup, K. Long and J. Borg, "The SmartPhantom: A beam profile and dose measuring device," 2021.

[30] M. T. Studenski and Y. Xiao, "Proton therapy dosimetry using positron emission tomography.," *World journal of radiology,* vol. 2, no. 4, p. 135–142, 2010.

[31] P. Casolaro, L. Campajola, G. Breglio, S. Buontempo, M. Consales, A. Cusano, A. Cutolo, F. Di Capua, F. Fienga and P. Vaiano, "Real-time dosimetry with radiochromic films," *Scientific reports,* vol. 9, no. 1, 2019.

[32] M. Kawashima, A. Matsumura, H. Souda and M. Tashiro, "Simultaneous determination of the dose and linear energy transfer (LET) of carbon-ion beams using radiochromic films," *Physics in Medicine & Biology,* vol. 65, no. 12, 2020.

[33] S. Vynckier, D. Bonnett and D. Jones, "Code of practice for clinical proton dosimetry," *Radiotherapy and Oncology,* vol. 20, no. 1, 1991.

[34] G. Knoll, Radiation Detection and Measurement, Wiley, 2010.

[35] L. Kelleter and S. Jolly, "A mathematical expression for depth-light curves of therapeutic proton beams in a quenching scintillator.," *Medical physics,* vol. 47, no. 5, pp. 2300-2308, 2020.

[36] J. B. Birks, The Theory and practice of scintillation counting., Pergamon Press Limited, 1964.

[37] R. Craun and D. Smith, "Analysis of response data for several organic scintillators," *Nuclear Instruments and Methods,* vol. 80, no. 2, p. 239–244, 1970.

[38] J. Lascaud, P. Dash and M. Würl et al., "Investigating the accuracy of co-registered ionoacoustic and ultrasound images in pulsed proton beams," *Phys. Med. Biol.,* vol. 66, 2021.

[39] S. Kellnberger, W. Assmann, S. Lehrack, S. Reinhardt and P. Thirolf et al., "Ionoacoustic tomography of the proton bragg peak in combination with," *Scientific reports,* vol. 6, 2016.

[40] J. Lascaud, R. Kalunga and M. Würl et al., "Applicability of Capacitive Micromachined Ultrasonic Transducers for the detection of proton-induced thermoacoustic waves," 2021.

[41] J. Lascaud, P. Dash and M. Würl et al., "Enhancement of the ionoacoustic effect through ultrasound and photoacoustic contrast agents," *Sci Rep,* vol. 11, no. 2725, 2021.

[42] J. Lascaud, R. Kalunga, S. Lehrack and e. al, "Applicability of Capacitive Micromachined Ultrasonic Transducers for the detection of proton-induced thermoacoustic waves," *IEEE International Ultrasonics Symposium (IUS),* pp. 143-146, 2019.

[43] LhARA Collaboration, "The LhARA initiative," 02 10 2021. [Online]. Available: https://ccap.hep.ph.ic.ac.uk/trac/raw-attachment/wiki/Research/DesignStudy/2021-10-02-LhARA-Brief-Final.pdf.

[44] LhARA Collaboration, "LhARA: The Laser-hybrid Accelerator for Radiobiological Applications," *Frontiers in Physics* , vol. 8, 2020.

[45] S. Zarifi, H. Taleshi Ahangari, S. Jia, M. Tajik-Mansoury, M. Najafzadeh and M. Firouzjaei, "Bragg peak characteristics of proton beams within therapeutic energy range and the comparison of stopping power using the GATE Monte Carlo simulation and the NIST data.," *Journal of Radiotherapy in Practice,* vol. 19, no. 2, pp. 173-181, 2020.

[46] NIST, "PSTAR : Stopping Power and Range Tables for Protons," [Online]. Available: https://physics.nist.gov/cgi-bin/Star/ap_table.pl. [Accessed 08 04 2023].